Spacecraft surface charging induced by severe environments at geosynchronous orbit

J.C. Matéo-Vélez, A. Sicard, D. Payan, N. Ganushkina, N.P. Meredith, I. Sillanpäa

Spacecraft surface charging induced by severe environments at geosynchronous orbit

J.-C. Matéo-Vélez[1], A. Sicard[1], D. Payan[2], N. Ganushkina[3,4], N. P. Meredith[5] and I. Sillanpää[3]

[1]ONERA - The French Aerospace Lab, Toulouse, France

[2]Centre National d'Etudes Spatiales, Toulouse, France

[3]Finnish Meteorological Institute, Helsinki, Finland

[4]University of Michigan, Ann Arbor, MI, USA

[5]British Antarctic Survey, Cambridge, UK

Corresponding author: J.-C. Matéo-Vélez, 2 avenue Edouard Belin, 31000 Toulouse, France (Jean-Charles.Mateo_Velez@onera.fr)

Key Points:

- A new set of severe space environments is compared to satellite surface charging mitigation guidelines at geosynchronous orbit
- New severe environment electron spectra exceed the guidelines by up to a factor of 10 below 10 keV
- Satellites anomalies previously reported are concomitant with the injection of high fluxes of electrons between 10 and 50 keV

This article has been accepted for publication and undergone full peer review but has not been through the copyediting, typesetting, pagination and proofreading process which may lead to differences between this version and the Version of Record. Please cite this article as doi: 10.1002/2017SW001689

Abstract

Severe and extreme surface charging on geosynchronous spacecraft is examined through the analysis of 16 years of data from particles detectors on-board the Los Alamos National Laboratory spacecraft. Analysis shows that high spacecraft frame potentials are correlated with 10 to 50 keV electron fluxes, especially when these fluxes exceed 1×10^{8} $cm^{-2}s^{-1}sr^{-1}$. Four criteria have been used to select severe environments: 1) large flux of electrons with energies above 10 keV, 2) large fluxes of electrons with energies below 50 keV and above 200 keV, 3) large flux of electrons with energies below 50 keV and low flux with energies above 200 keV, and 4) long periods of time with a spacecraft potential below - 5kV. They occur preferentially during either geomagnetic storms or intense isolated substorms, during the declining phase of the solar cycle, during equinox seasons and close to midnight local time. The set of anomalies reported in *Choi et al.* [2011] is concomitant with a new database constructed from these events. The worst-case environments exceed the spacecraft design guidelines by up to a factor of 10 for energies below 10 keV. They are fitted with triple Maxwellian distributions in order to facilitate their use by spacecraft designers as alternative conditions for the assessment of worst-case surface charging.

1. Introduction

Charged particles in space are known to jeopardize spacecraft and are believed to be responsible for a significant fraction of spacecraft anomalies ranging from temporary outage to power or function losses [*Baker*, 2000; *Iucci et al.*, 2005].The interaction between components and a particle depends on the particle type and energy. Galactic cosmic rays and solar energetic ions can penetrate the satellite shielding surfaces and generate single event effects such as phantom commands on electronic components. Relativistic electrons (E > ~ 500 keV) can also penetrate the satellite shielding leading to internal charging and electrostatic discharges (ESDs). The susceptibility of electronic systems to electromagnetic compatibility (EMC) issues may be exceeded and it may generate sporadic losses of functions. For example, three geostationary spacecraft (ANIK E1, E2 and Intelsat K) began to spin out of control on the same day of January 1991 due to ESDs caused by a geomagnetic storm [*Leach*, 1995]. It required several hours for backup systems to be activated and for fully nominal operations to be restored, except on ANIK E2 which was only fully restored 3 years later. Studies have shown a significant correlation between satellite anomalies thought to be caused by ESDs and increased fluxes of relativistic electrons [*Wrenn*, 1995; *Wrenn et al.*, 2002]. This process, however, needs a certain amount of time for the charge to build-up, since the spacecraft shielding reduces significantly the electron fluxes below a fraction of $pA.cm^{-2}$ at geosynchronous orbit (GEO) and at Medium Earth Orbit (MEO). It is thus not always possible to relate the occurrence of such disastrous events with space weather conditions, unless detailed analysis of environmental history is used as input of internal charging modeling [e.g., *Ryden and Hands*, 2017]. On the other hand, a series of anomalies at GEO have been attributed to electrons and protons of energy below 100 keV, responsible for surface charging.

Extreme spacecraft charging conditions of the order of −10kV were first recorded by geosynchronous satellites ATS 5 and ATS 6 [*DeForest*, 1972, 1973]. It was shown that most of severe charging events were measured during eclipse and high Kp index [*Garrett*, 1981]. Surface charging is the result of a complex interaction between the spacecraft and its plasma environment [e.g., *Lai*, 2011]. At GEO in eclipse, the main contribution to spacecraft potential is the ambient electron current, especially during electron flux enhancement by geomagnetic storms and sub-storms. At GEO in sunlight, the largest contribution to

spacecraft potential is the emission of electron by UV photon impacts. Photoemission makes fully conductive spacecraft charge to a few volts positive, which is enough to attract back photoelectrons of a few eV and reach current balance. Some surprising exceptions have nevertheless been reported by *Sarno-Smith et al.* [2016] when the fully conductive Van Allen Probes spacecraft charged down to a few hundreds of volts negative in sunlight. Frame potential (relative to the ambient plasma environment) is an important parameter in the assessment of charging risks but the most important parameter is differential charging of surface materials, as e.g., insulating coverings, relative to the structure or frame. Materials with different electrical properties (electron random reflection and electron emission by surfaces impacted by electron, proton and photons) charge differentially with respect to each other and to the spacecraft frame. Shaded insulators can charge negative independently from the frame potential as reported on SCATHA for example, where constantly shadowed insulators charged a few hundreds of volts negative [*Mizera*, 1981]. Sunlit insulators charge positive with respect to the frame due to photoemission. In addition, they modify the frame potential by reducing the area of sunlit conductive material. Not fully conductive spacecraft may thus charge negative in sunlight and during electron flux enhancements, as recorded for example on SCATHA [*Gussenhoven and Mullen*, 1983]. A typical configuration at GEO consists in telecom spacecraft with large solar panels covered with insulating cover glasses. Sunlit cover glasses tend to charge less negative because of intense photoemission. This situation is likely to trigger electrostatic discharges, in the so-called triple point configuration where a negative conductive structure is in contact with a less negative insulator and vacuum [*Cho and Hastings*, 1993: *Payan et al.*, 2001].

Even though modern satellites have benefited from the analysis of past flight anomalies and losses [*Koons et al.*, 2000], surface charging remains a source of problems [*Minow and Parker*, 2014; *Ferguson*, 2016]. A statistical analysis of the 95 commercial satellite anomalies provided by the Satellite News Digest (SND) website in the period of 1997–2009 showed the anomalies have a strong correlation with geomagnetic activity as monitored by the Kp index [*Choi et al.*, 2011; *Choi et al.*, 2012]. Even though *Mazur and O'Brien* [2012] indicated that a number of these anomalies were not related to the environment, the combined detailed analysis of Los Alamos National Laboratory (LANL) GEO spacecraft data made by *Choi et al.* [2011] and by *Thomsen et al.* [2013] indicated that anomalies are more likely to occur a) during higher values of Kp index, b) in the local time between premidnight through dawn; c) during the equinox seasons; d) during the declining phase of the solar cycle. This is consistent with surface charging by particles of energy below a few tens of keV, even though the mechanism leading to the spacecraft anomalies was not fully understood.

Current spacecraft design guidelines provide valuable information on the mitigation techniques to be used to limit the occurrence of ESDs and to ensure they do not generate detrimental effects. One aspect of the guidelines produced by the European Cooperation for Space Standardization (ECSS) and by the National Aeronautics and Space Administration (NASA) concerns the definition of worst-case environments in the Earth magnetosphere for surface charging [*ECSS*, 2008; *NASA*, 2011]. They are currently based on the data obtained in the 1970's and 1980's [*Purvis et al.*, 1984], especially onboard the SCATHA and ATS-6 satellites. The low energy electron and proton distribution functions measured at GEO were fitted by double Maxwellian distribution functions to facilitate their use by engineering tools such as computational models whose modern versions are SPIS [*Roussel et al.*, 2012; *Thiébault et al.*, 2016], NASCAP-2k [*Mandell et al.*, 2006] and MUSCAT [*Muranaka et al.*, 2008].

The main question for spacecraft designers is to determine which environments they should rely on to assess worst-case charging estimations, especially at GEO. Efforts were thus made to assess worst-case surface charging environments using 3D numerical simulations of the spacecraft interaction with the environment [*Ferguson and Katz*, 2014; *Mateo-Velez et al.*, 2016a]. To provide more inputs to a possible revision of standards and guidelines, it was judged necessary to extend the range of flight data used to define worst-case conditions. A first attempt was made by *Cho and Nozaki* [2005], but their analysis of LANL data based on moments of particle distributions and spacecraft potential provided routinely, was significantly biased by some incorrectly-calculated moments. As indicated by *Ferguson and Katz* [2014], LANL acknowledged erratic points given by the automatic post-processing procedure that computes the moments. In addition, moments provide less information than spectra. It was shown by the same team that using electron and proton spectrograms leads to a better estimation of the spacecraft potentials [*Oda et al.*, 2016]. An exhaustive analysis of 13 years of LANL spectrograms showed that spacecraft potentials below -100 V correlate with the 8 keV electron flux exceeding 1.4×10^3 $cm^{-2}s^{-1}sr^{-1}eV^{-1}$ [*Thomsen et al.*, 2013]. This threshold may be used by space weather situational tools to provide alerts and warnings based on models or observations of the low energy electron fluxes in geosynchronous orbit and help spacecraft operators applying mitigation techniques. At the spacecraft design phase, however, there is still a need for full electron and ion spectra definitions during severe conditions. Finally, electron flux limits have been estimated by *O'Brien et al.* [2007] using 11 channels of LANL sensors from 63 keV up to 4.75 MeV. They determined the maximum flux at each energy bin by observing many nonoverlapping intervals of several hours to several days. Even though the authors provided bound limits of electron fluxes, actual spectra are required by spacecraft designers to assess surface charging [*Rodgers et al.*, 2016].

It is important to stress that spacecraft charging is complex. As introduced above, it depends not only on the environment, but also on spacecraft geometry and material properties. Differential charging and subsequent ESD risk is also driven by three-dimensional barriers of potentials [*Purvis*, 1983]. Consequently, the worst-case environment for one satellite design will likely be different from the worst-case environment for another satellite.

The main objective of this paper is to propose a new set of severe GEO environments for surface charging analyzing 16 years of LANL data based on reasonable criteria and to compare the results with current guidelines. We also use the POES data to compare and contrast the results obtained at high altitude by the LANL satellites at GEO with those at low altitude in LEO on field lines that map to GEO. The second objective is to compare the results with the list of anomalies from *Choi et al.* [2011]. We first present our data post-processing method in Section 2. Then, through a statistical analysis, we correlate surface charging levels to low energy electron fluxes, in Section 3, and examine the characteristics of severe events in Section 4. Section 5 presents a selection of LANL worst-case conditions that is compared to standards from guidelines in Section 6. Finally, the main conclusions and recommendations are developed in Section 7.

2. Observations

Instruments on-board the spinning LANL spacecraft measure the electron and ion fluxes from a few eV up to several MeV. The Magnetospheric Plasma Analyzer (MPA) measures low energy particles from 1 eV to 40 keV [*Bame et al.*, 1993] but only 100 eV to 40 keV bins are used in this paper because lower energy bins may be subject to contamination. This contamination is illustrated in figure 1 of *Thomsen et al.* [2013] by an "*intense population of low-energy electrons (below ~10 eV) which are predominantly photoelectrons*

and secondary electrons produced on the spacecraft and trapped near the surface by differential potentials that develop within the charging sheath". The Synchronous Orbit Particle Analyzer (SOPA) measures particle fluxes between 50 keV and 1.3 MeV [*Belian et al.*, 1992]. At the highest energies, the Energetic Spectra for Particles (ESP) measures particle fluxes from 1 to several MeV [*Meier et al.*, 1996]. In the present paper, LANL-01A data have not been used because of large uncertainties in its MPA instrument. The LANL satellites used in this study, together with the time periods covered by MPA, SOPA and ESP detectors, are presented in Table 1. Data have been initially filtered to remove contamination, noise and glitches and have been inter-calibrated [*Sicard-Piet et al.*, 2008; *Lazaro et al.*, 2011]. The time resolution of MPA is 86 seconds, while the time resolution of SOPA and ESP is 10 seconds. The SOPA and ESP measurements have been averaged over 86 s. The spacecraft potential routinely provided by LANL is to some extent different from that computed by *Thomsen et al.* [2013] who use only the ion peak line which is clearly visible on the ion spectra when the spacecraft charges negative. Ions are accelerated by the electric field directed towards the spacecraft. They get an additional kinetic energy before impacting the sensor. It results in filling the MPA energy bins close to the spacecraft potential with low energy ions fluxes. The potential provided routinely by LANL is based first on the detection of the ion line. If this automatic procedure fails, an analytical formula is used to obtain it from the moments of the electron distribution. This is described in *Thomsen et al.* [1999] and in *Davis et al.* [2008] and has been confirmed by M. Thomsen [private communication].

Figure 1 presents proton differential fluxes measured during two charging events on LANL_1994_084 on 2004/4/5 at 19:21:19 UTC and on LANL_1991_080 on 1997/3/13 at 19:04:22 UTC. The peaks around 700 eV and 5 keV corresponds to potentials of -700 V and -5 kV respectively. In this paper, the proton differential flux is scanned starting from the highest energy to optimize the automatic detection of the ion line peak. The scan starts at 9 keV and moves down in energy. It limits the uncertainties linked to noise on low energy bins, except when the cold ion population is very small. From the examples shown in Figure 1 this automatic detection seems more adapted to high negative potentials. This automatic detection of the potential differs from that of LANL which provides either a) the potential given by the ion peak method or b) the potential given by an analytical formula based on the moments of the distribution functions when method a) fails to provide an answer. Even though method b) efficiently fits method a) on the major part of the data, a non-negligible amount of the results significantly over estimate the actual potential given by method a). Therefore, to avoid the possibility of using an overestimation of the potential we use a method based on method a) [*Thomsen et al.*, 2013]. In this paper, the method used to find the proton peak is based on the ratio between the flux at a given energy and the flux at a nearby energy. For each measurement (every 86s), this ratio is calculated for each energy range between 1 eV and 9 keV. In order to have a valid determination of the potential this ratio must be at least equal to 2. The greatest energy for which this ratio is greater than 2 is considered to be equal to the absolute value of the satellite potential. The upper bound of this algorithm is 9 keV because previous examinations showed large uncertainties above this value [*Mateo-Velez et al.*, 2016b].

Figure 2 shows the number of measurements, over 16 years of LANL data, which are associated with a given potential as provided by the ion peak method and to a given potential as provided routinely by LANL. If the two techniques were absolutely similar, one would obtain points on the identity curve only. The consistency of results is clearly visible except on a number of data which are believed to come from the limitations of method b). The scatter on both sides of the identity curve suggests that the ion line method may also overestimate

the potential dramatically at times. Therefore, visual inspection of spectra is sometimes necessary.

In the present paper, the potentials obtained with method a) have been used to correct the particle differential fluxes using Liouville's theorem that allows accounting for the effect of a negative spacecraft potential that results in electron repulsion and proton acceleration [*Deutsch*, 1982; *Mateo-Velez et al.*, 2016a]. The impact of potentials below -1 kV on electron fluxes of energy below 10 keV is visible in the statistical analysis made by *Thomsen et al.* [2013] and presented in their figure 4. The tilted shape of the electron fluxes increases with decreasing energies, which makes it difficult to use low energy bins for a direct correlation with the satellite potential. For instance, electrons measured in the 311 eV bins when the spacecraft was charged to -1 kV represent electrons in the undisturbed plasma with energy of around 1300 eV. *Thomsen et al.* [2013] used the spacecraft potential to correct the moments of the distribution functions but they did not use the Liouville's theorem to correct the differential fluxes (M. Thomsen, private communication), which can make it difficult to interpret low energy electron fluxes, below 5 keV. The 8 keV and 13.5 keV bins are much less impacted by the electric field distortion. As a result, in this paper, we use the ~10 keV bin as the lower bound of our statistical analysis. Using method a) is the main difference with our previous work [*Mateo-Velez et al.*, 2016a] which was based on results from method b), subject to caution due to the reasons expressed earlier in this section. Indeed, we showed that method b) can produce significant distortion with respect to method a) during charging events [*Mateo-Velez et al.*, 2016b].

In addition to LANL data, we use the electron fluxes measured on the NOAA/POES satellites in Low Earth Orbit (LEO) from 1998 to 2014. Specifically, we use the POES data for event studies and for the computation of selected exceedance levels for comparison with the LANL events and ongoing POES events. The orbits of each of these satellites cross field lines that map out to geosynchronous orbit four times per orbit. For this study we used a database of the maximum 2 second electron flux observed in any given 3 hour window, in a given energy range (E > 30 keV, E > 100 keV, E > 300 keV) as a function of L* as detailed in *Meredith et al.* [2016]. The database was first examined to compute the average and exceedance levels, that is, the fluxes that are exceeded by only a given fraction of the data. At L* = 6.0 at LEO, the mean and the 5%, 1% and 0.1 % exceedance levels of the fluxes above 30 keV are 1.89×10^6, 9.24×10^6, 1.73×10^7 and 2.98×10^7 $cm^{-2}s^{-1}sr^{-1}$, respectively. The database was also used to examine the evolution of the electron flux during specific events identified by the LANL satellites.

3. Statistical Results

The electron fluxes have been sorted into four energy bins: 10-50 keV; 50-100 keV; 100-200 keV and above 200 keV.

Figure 3 shows the distribution of the integral flux between (a) 10 and 50 keV and (b) 50 and 100 keV. We show the distribution in terms of the exceedance level, where the X% exceedance level is defined as the integral flux over a given energy range that is exceeded by only X % of the data. The mean flux and selected exceedance flux levels are highlighted by colored lines in each panel. The mean flux and the 89%, 10 %, 1% and 0.01 % exceedance fluxes between 10 and 50 keV are 1.5×10^7, 1.0×10^6, 4×10^7, 1×10^8 and 2×10^8 $cm^{-2}s^{-1}sr^{-1}$, respectively. The mean flux and the 82%, 10 %, 1% and 0.01 % exceedance fluxes between 50 and 100 keV are 4×10^6, 1.0×10^6, 8×10^6, 3.2×10^7 and 1.15×10^8 $cm^{-2}s^{-1}sr^{-1}$, respectively.

Figure 4 presents the number of 86 s averaged data with a given potential and with a given electron flux between (a) 10 and 50 keV and (b) 50 and 100 keV. Only the negative potentials are represented (by their absolute values). Ion spectra with no peak are related to positive spacecraft charging, typical of spacecraft in sunlight during quiet environmental conditions. These events are not plotted in Figure 4. The probability to reach a few hundreds of volts of negative charging increases sharply with 10-50 keV fluxes above the average flux of 1.5×10^{7} $cm^{-2}s^{-1}sr^{-1}$ (represented by the dashed line in Figure 4a). On the other hand, a large number of events with high charging levels occurred with 50 to 100 keV fluxes below the average flux of 4×10^{6} $cm^{-2}s^{-1}sr^{-1}$ (also represented by the dashed line in Figure 4b). This is quantitatively confirmed in Figure 5 which presents the probability to reach a potential below a given negative potential exceeded for (a) 10 to 50 keV and (b) 50 to 100 keV fluxes between two selected exceedance levels. Most events are associated with very limited potentials above -1 V. Fluxes of 10-50 keV electrons in the range 1×10^{8}-2×10^{8} $cm^{-2}s^{-1}sr^{-1}$, corresponding to exceedance levels in the range 1%-0.01%, result in potentials below -1kV ~10% of the time, which is considered in this paper to increase the ESD risk to a significant level. At even higher flux levels, fluxes of 10-50 keV electrons in the range 2×10^{8}-7×10^{8} $cm^{-2}s^{-1}sr^{-1}$, corresponding to exceedance levels in the range 0.01%-0.0001%, result in potentials below -1kV ~22% of the time, which is considered in this paper to increase the ESD risk to a high level. From Figure 4a), there are very few events above the 0.01 % exceedance flux level. These events are split between low charging levels (above -1 V) and strong negative charging levels (below -1000 V). In sharp contrast fluxes of 50-100 keV electrons with exceedance levels in the range 1%-0.1% and 0.01%-0.001% have probabilities less than 0.3 % and less than 1% to reach -1kV or below.

The best correlation with potentials is thus obtained for 10-50 keV electrons, which is consistent with the 8 keV and 9 keV electron temperature thresholds from *Thomsen et al.* [2013] and from *Ferguson et al.* [2015], respectively. Previous results showed that frame charging of the SCATHA spinning spacecraft correlated with the electron flux above the threshold temperature of 30 keV [*Mullen et al.*, 1986]. The theoretical reasons for a threshold temperature based on the interaction of the secondary electron yield of materials with a single maxwellian temperature environment was described by *Lai* [2011] based on previous papers. A correlation with the cold ion distribution is also expected by *Gussenhoven and Mullen* [1983] because, depending on its density and temperature, it can limit the negative charging due to strong focusing of low energy particles towards negatively charged spacecraft surfaces. The large effect of spacecraft potential on < 100 eV protons makes it difficult to have a clear picture of it, however. In the present work, it was decided to retain Liouville's corrected ion fluxes only at energies above twice the ion peak energy. This enables the removal of the strong uncertainties associated with the conversion of the measured ion flux around the ion peak to initial distribution function.

The 10 to 50 keV electron flux thresholds above may be used as an indicator of surface charging risks at GEO. This was proposed in the frame of the SPACESTORM project funded by the European Union's 7th Framework Program to model space weather events and mitigating their effects on satellites (http://www.risk.spacestorm.eu/).

4. Severe Environments Characteristics

There are various ways of defining severe environments. In this paper, we have used four criteria. As shown in the previous section, electron integral fluxes between 10 and 50 keV provide valuable information on the severity of space environments on a real spacecraft.

As a result, we have defined three criteria for defining severe conditions based on integral fluxes and a fourth criterion based on the measured spacecraft potential. For each of the first three criteria, the electron and protons fluxes have been averaged over 15 minutes, on one hand, and over 86 seconds, on the other hand, because severe conditions need to remain over a few minutes for differential charging to occur in geosynchronous orbit. For instance, a 100 µm thick insulator submitted to an electron flux of 2×10^8 $cm^{-2}s^{-1}sr^{-1}$ charges up to ~-1 kV with respect to the frame within ~100 s, neglecting secondary electron emission. For the sake of conciseness, we present 15 minutes average data in this section.

The first criterion concerns the highest Fluxes of electrons at Energies above 10 keV (FE10k). The second criterion concerns the Highest Fluxes at All Energies (HFAE). It combines high fluxes both below 50 keV and above 200 keV which is thought to be related to charge deposited both at the surface and in the bulk of covering insulators. The algorithm used to select these spectral shapes consists first in normalizing the integral fluxes below 50 keV and above 200 keV to get $\hat{f}_{<50keV}$ and $\hat{f}_{>200keV}$ in the interval (0; 1] and in maximizing the value of $\sqrt{log^2(\hat{f}_{<50keV}) + log^2(\hat{f}_{>200keV})}$. The third criterion concerns high fluxes at low energies together with a Low Flux at High Energy (LFHE). It combines both high fluxes below 50 keV and low fluxes above 200 keV which is related to surface charging. The same algorithm as for HFAE is used except $\hat{f}_{>200keV}$ is replaced by the ratio between the flux below 50 keV and the flux above 200 keV. A simple declustering technique was used to avoid the detection and selection of several spectra within the same event (that can last a few hours or even days). The most severe electron spectrum was selected each month on each spacecraft, the latter allowing assessing if some events were detected by several spacecraft. The list of most severe satellite-month spectra was then classified within three top 100 series - one for each criterion.

The fourth criterion extracts the average spectra related to large negative potentials over long periods of time. From Figure 2, the minimal potential over 16 years of LANL data is around -8 kV but is only associated with a few events. In this paper, we consider the longest events with a Potential Greater than 5 kV - in absolute - (PG5k). This criterion hence focuses on events associated with large negative potential that give plenty of time for differential charging to occur.

Table 2 presents the minimum and maximum values of the 8 keV differential electron flux, and the minimum and maximum values of the 10 to 50 keV integral electron flux of the FE10k, HFAE, LFHE and PG5k top 100 events. It also presents the minimum, maximum and average potentials of the FE10k, HFAE and LFHE top 100 events. The 8 keV differential fluxes all exceed the threshold of 1.4×10^3 $cm^{-2}s^{-1}sr^{-1}eV^{-1}$ given by *Thomsen et al.* (2013) that assessed charging conditions below -100 V. The 10 to 50 keV electron flux ranges from 1.2 to 2×10^8 $cm^{-2}s^{-1}sr^{-1}$ for FE10k events which, following Figure 5, corresponds to a statistical risk of around 10 % to get a potential below -1 kV. The 10 to 50 keV electron flux ranges from 0.2 to 1.4×10^8 $cm^{-2}s^{-1}sr^{-1}$ for HFAE events which corresponds to a statistical risk ranging from almost no risk to 10 % to get a potential below -1 kV. The 10 to 50 keV electron flux ranges from 0.5 to 1.6×10^8 $cm^{-2}s^{-1}sr^{-1}$ for LFHE events which corresponds to a statistical risk ranging from 1% to 10 % to get a potential below -1 kV. On average, the LANL potential during the FE10k, HFAE and LFHE top 100 events is -600, -800 and -500 V respectively, which is consistent with the statistical results above. There is, however, a large dispersion in the potential from almost no charging in a few cases down to thousands of volts of negative charging. This dispersion was also observed in *Thomsen et al.* [2013]. Figure 6 puts together histograms obtained with the four criteria. Each column of the histograms

cumulates the number of events with a given property, starting from FE10k (in blue), then adding HFAE (in red), LFHE (in green) and finally PG5K (in purple). The size of any given color bar represents the number of occurrences. On each panel and for each criterion, the sum of events over all the columns is 100. Figure 6a presents the number of occurrences of potentials between 0 and -8 kV. Figure 6b presents the number of occurrences each year from 1989 to 2005. It also shows the number of LANL spacecraft each year with their start and end time (if they come to an end). Figure 6c presents the number of occurrences each month from January to December. Figure 6d presents the number of occurrences at each local time between 0 to 24 MLT. Finally, Figure 6e presents the number of occurrences of Kp index between 1 and 9. It also shows the frequency of occurrence of Kp in % over the 16 years of data.

Most events occurred in the 21-06 MLT sector with a few occurrences in the 07-08 MLT sector and at 20 MLT, which is consistent with previous studies [*e.g., Mullen et al.,* 1986]. It is important to stress that all PG5k events are concentrated around midnight. Even though the occurrence rate of the higher Kp indexes (6-9) over the 16 years reaches about 2%, they are related to a much higher percentage of the charging events (74/400). This is consistent with prior studies that showed a consistent up trend of frame potential with higher Kp [*Garrett*, 1981]. Both the location and the geomagnetic activity dependence show good agreement with the global maps of low energy electrons observed during the CRRES mission [e.g. *Meredith et al*., 2004; *Bortnik et al.,* 2007]. The higher occurrence observed from 2003 to 2005 is in agreement with *Thomsen et al.* [2013], but it is however quite unusual since an 11-12 year solar cycle dependence was expected. As the number of geomagnetic storms varies over the cycle, this plot should have a sinusoidal envelope. The number of spacecraft hosting LANL sensors was multiplied by 2.5 between 1991-1993 and 2003-2005, which does not explain the increase in the number of events by a factor of 5 to 8. The jump in the last three years may perhaps reflect a change in the host spacecraft designs that changes the charging response. Seasonal effects are observed, especially for the PG5K top events, with a higher occurrence in March and September. The other cases of environments exhibit a higher occurrence near equinoxes and a lower occurrence near solstices, which is consistent with variations in geo-effectiveness of solar storm triggers of the geomagnetic storms and substorms that produce the highest fluxes of energetic electrons [*Russell and McPherron*, 1973]. The same seasonal dependence was observed by *Wilkinson* [1994] concerning the occurrence of phantom command anomalies on GOES satellites. These anomalies were attributed to differential surface charging caused by energetic electrons injected during geomagnetic substorms.

Around 80 events out of the FE10k top 100 events induced a potential equal or below -300 V, which is significant in terms of surface charging risks. 12 events were below -1 kV, which is in agreement with the statistical analysis presented earlier predicting that around 10% of the events induced a potential below -1 kV. Around 60 events out of the HFAE top 100 events induced a potential equal or below -300 V. 16 events were below -1 kV. 3 events were below -5.2 kV, all of which occurred when the spacecraft was in Earth shadow, *i.e.* close to local midnight and in equinox season (Feb-March; Sept-Oct). Around 40 events out of the LFHE top 100 events induced a potential equal or below -300 V. 4 events were below -3.9 kV, all of which occurred when the spacecraft was in Earth shadow. With respect to FE10k events, the HFAE and LFHE events produced a non-negligible number of low charging levels with a potential between -300 V and 0 V. The FE10k criterion agrees with the previous analysis of Figure 4 and Figure 5 since large electron fluxes between 10 and 50 keV are statistically correlated with large negative potentials. Severe charging also occurs during the most severe HFAE and LFHE conditions but with a lower probability. The PG5k top 100

events all occurred when the spacecraft was in eclipse with an average potential of -6 kV, even for limited geomagnetic activity (Kp ≤ 3). Spacecraft are more susceptible to charge to highly negative potentials in eclipse because of the absence of photoelectron emission. The occurrence of charging events below -5kV is dominated by PG5k cases, whereas the other cases produce potentials around or above -1 kV. Eclipses occur around the equinoxes, which explains the seasonal dependence for PG5k cases.

Figure 7 presents the duration of PG5k events as a function of the eclipse duration on the same day (ranging from 0 for no eclipse to 72 minutes at equinoxes). The longest event was 46 minutes. Statistically, the majority of PG5k events were observed when the spacecraft was in eclipse. 82 events out of 100 occurred in eclipse and lasted less than the eclipse duration. 5 events out of 100 occurred in eclipse and lasted longer than the eclipse duration. 13 events out of 100 occurred out of eclipse. These results clearly confirm that the response of a spacecraft to the space environment is very different in sunlight and in eclipse. Further work beyond the scope of this paper should separate eclipse and non-eclipse charging data and examine the most severe events for the two cases.

The database can also be used to examine the timing of the events with respect to storms and substorms. All the events (400) with all four criteria were attributed with the corresponding values of Dst and AE indices and those indices were analyzed during time periods around the detected surface charging events in order to determine if there was any associated substorm or storm activity. For storms, we identified the initial, main and recovery phases based on the Dst-index variations. Substorm activity was separated into isolated moderate substorms (AE-index from 300 nT to 800 nT) and isolated intense substorms (AE-index higher than 800 nT). If a substorm occurred during storm, it was not counted as an isolated substorm. Our findings are shown in Figure 8.

Almost all the FE10k events occurred during storm initial, main or recovery phases or during intense isolated substorms. The HFAE events mainly occurred during substorms periods. The LFHE events were equally distributed between storms and sub-storms periods. Finally, half of the PG5k events occurred during moderate substorms. These results show that it is not necessary to have extreme conditions to get severe spacecraft surface charging. The eclipse situation is efficient at provoking long periods of times with high negative voltage even with moderate plasma conditions.

Figure 9 presents the number of occurrences of NOAA/POES fluxes that exceeded the average and the exceedance levels - discussed in Section 2 - during the FE10k, HFAE, LFHE and PG5k top 100 events (colored as in Figure 6). The size of any given color bar represents the number of occurrences. For each criterion, a total number of 100 events are plotted. Each column groups the number of occurrences of events with a flux comprised between the flux given in abscissa and the flux next to its right. The plot concerns the fluxes of electrons of energies above 30 keV at LEO and at L* = 6.0. We select data that are not contaminated by solar protons. Using the Space Weather Prediction Center definition of a solar proton event, we exclude the intervals whenever the flux of E > 10 MeV protons determined from GOES is greater than 10 $cm^{-2}s^{-1}sr^{-1}$. This results in the selection of a total number of 249 out of 400 events. Out of these 249 events, 226, 106, 33 and 3 events exceeded the average flux, the 5% exceedance level, the 1% exceedance level and the 0.1% exceedance level respectively. Almost half of the registered events are thus correlated with a significant enhancement of E >30 keV electron fluxes at LEO and at L*= ~ 6.

The space environment is likely to induce some anomalies on satellites orbiting close to the LANL spacecraft. Table 3 presents a list of LANL events out of FE10k, HFAE, LFHE and PG5k top100 series that are concomitant to 11 out of the 95 anomalies reported by *Choi*

et al. [2011]. The panel on the left is reproduced from *Choi et al.* [2011], including the original number in the anomaly list. No precise timing information is provided for many anomalies. The anomalies occurred for Kp > 5. Anomalies may be classified in two sets: (1) temporary outage or equipment failure for anomalies 22, 24, 45, 55, 58, 60; and (2) power losses for anomalies 1, 13, 35, 43, 56. The panel on the right presents a LANL event that appears to be concomitant with these anomalies.

The first set of anomalies, referred as (1) in Table 3, could possibly be related to high energy electrons responsible for temporary outage, because enhanced FE10k and HFAE fluxes are concomitant on LANL around the same periods of time. This is consistent with internal charging produced by electrons above a few hundreds of keV, while at the same time not being able to rule out single event effects generated by solar ions above a few MeVs. This would require further analysis.

The second set of anomalies, referred as (2) in Table 3, may be linked to low energy plasma - inducing electrostatic discharges, for instance. Electrostatic discharges on solar panels can generate arcing between solar cells and produce power losses. Arcing on power cable harness is also a concern. For instance, the failure of the Advanced Earth Observation Satellite (ADEOS) II occurred at low altitude of 800 km in the auroral zone made very active with high flux of > 30 keV electrons during the "Halloween event" on October 24, 2003 due to a Coronal Mass Ejection [*Cho*, 2005]. The loss was attributed to power cable harness arcing [*Maejima et al.*, 2004]. The anomaly 43 of Table 3 that led to the loss of a satellite occurred near several long periods of potentials below -5 kV on LANL a few days before and after. Without any further detail on the anomalies, we advise caution on the interpretation of the results. We highlight, however, that they are concomitant with low energy plasma injection events measured on LANL around the same period of time.

5. Worst-Case Environments

Worst-case conditions for surface charging can be selected out from the top 100 series above by considering the environment ranked number 1 for each criterion. Table 4 presents the characteristics of the worst case environments including the spacecraft, the date, the local time, the Kp index, the electron differential flux at 8 keV, the electron integral flux between 10 and 50 keV and the spacecraft average potential. Each of the '15 min' FE10k, HFAE and LFHE worst-case environments is the average of ten consecutive measurements 86 seconds each. Each of the 86 seconds FE10k, HFAE and LFHE worst-case environments is the worst spectra in its category. The PG5K worst-case is also presented in this table using 46 minutes averaged data. The environment distributions presented in Table 4 have been checked by visual inspection in order to confirm the potential given by our automatic detection of the ion line peak.

The FE10k-15min worst-case event was measured on LANL-1994-084 on April 5th, 2004 at 1921 UTC, at 5.1 MLT, with a Kp of 6.3 and with an average potential of -670 V. The proton flux measured at the start time is represented by the solid line in Figure 1. This event exceeded both the 0.01 % LANL exceedance electron flux between 10 and 50 keV and the 8 keV flux threshold from *Thomsen et al.* [2013]. Figure 10 presents the NOAA/POES > 30 keV electron flux measured at LEO and at L*~6 the same week and the average, 5%, 1% and 0.1 % exceedance fluxes over 16 years of data. The plot shows a sudden increase in the electron flux on April 5th between 1800 and 2100 UTC, which exceeds the 1% exceedance level. The FE10k-86s worst-case event was measured on LANL-1994-084 on May 15th, 2005 at 06:36 UTC. Even though the FE10k-86sec worst-case event occurred in apparently

more severe geomagnetic conditions (Kp of 8.3) and was associated with larger electron fluxes, it did not produce a significant potential on LANL_1994_084. It might have produced, however, more impact on another spacecraft since the potential is also dependent on the spacecraft shape and covering materials.

The HFAE-15min and HFAE-86sec worst-cases events both have produced significant charging levels, down to -1600 V, during very intense geomagnetic activity, Kp~8. The latter was measured on July 15th, 2000. It was related to the extremely powerful solar flare which occurred on July 14th, during the so-called Bastille day storm. During this event the magnetosphere became extremely compressed and eroded, causing 3 geosynchronous GOES satellites to enter the magnetosheath for an extended time period [*Raeder et al.*, 2001]. The passage of the sheath of this Coronal Mass Ejection (CME) lasted for several hours from ~14:30 until ~19:10 UTC. The IMF Bz strongly fluctuated and reached ~-20 nT several times. The IMF BZ turned strongly southward and reached a minimum of -60 nT at ~20:00 UTC. The Bastille day event is also ranked #3 in the FE10k-15min and FE10k-86sec top 100 events.

The LFHE-15min and LFHE-86sec both occurred close to 0300 local time during intense geomagnetic activity, Kp ~5-7. The large electron fluxes of between 10 and 50 keV, which exceed the 1% and 0.01% exceedance fluxes, respectively, are thought to be responsible for potentials dropping below ~-600 V. The 8 keV differential electron flux is ten times larger than the threshold given by *Thomsen et al.* [2013].

The longest PG5K event was 46 minutes on LANL_1991_080 on March 13th, 1997, centered on 1904 UTC, at 23.5 MLT and Kp ~ 2. The proton flux measured at the start time is represented by the dashed line in Figure 1. This event occurred in the eclipse period. That means that high charging levels below -5000 V can occur in eclipse even with moderate geomagnetic activity. Its duration was lower than the eclipse duration of 65 minutes that day.

For practical use by spacecraft engineers in charge of worst-case surface charging assessment, space environments are usually fitted by single or bi-Maxwellian distribution functions. To account for the full range of the energy distribution, especially the energetic tail, the worst-case environments above need, however, to be represented by Kappa distributions or by triple Maxwellian distributions. Table 5 presents the triple Maxwellian distribution parameters obtained for the FE10k, HFAE, LFHE and PG5k worst-case environments. It was chosen to check the relevance of each fit by visual fit of the velocity and energy distribution functions, both in logarithm and linear scales, because automatic fits are likely to deform parts of the spectra.

6. Discussion

Figure 11(a) compares the worst-case electron differential fluxes obtained by the various methods described in the paper to the LANL average, to the AE8 min [*Vette*, 1991] and IGE 2006 [*Sicard-Piet et al.*, 2008] environment specification at GEO, and to the limiting fluxes determined from LANL observations [*O'Brien et al.*, 2007]. The worst case results are shown for both 15 minutes data (solid lines) and 86 s data (dashed lines). The LANL worst-case environments selected in the paper cross each other around 20 to 40 keV. Below 20 keV, the FE10k worst-case environments exceed LFHE by a factor lower than 2, HFAE by a factor of up to 5, and the AE8min and IGE environments by a factor of up to 20. Between 40 keV and 200 keV, the HFAE worst-case environments exceed AE8min, IGE and FE10k by a factor of up to 30, and LFHE by a factor of up to 1000. Above 200 keV, HFAE exceed FE10k and LFHE by a factor of 10 to 1000. The "O'Brien 2007" spectrum is the

worst 1 hour interval on LANL spacecraft for each energy bin. It exceeds HFAE by a factor up to 2 between 60 and 400 keV and by a factor up to 10 above.

The proton fluxes measured during the worst-cases above are presented in Figure 11(b), using the same average periods of 15 minutes and 86 seconds. They are compared to the average proton flux over 16 years of LANL data. Except for the FE10k-86sec worst-case, that exceeds other by a factor of up to 10, the proton fluxes are similar to or less than a factor of 3 greater than the average flux, below 200 keV. Above 200 keV, the proton fluxes depart from the average value. Even though the proton flux tends to exceed the average flux, further investigation would be necessary to get a clearer picture of their impact on spacecraft potential.

The FE10k, HFAE and LFHE worst-cases presented in Figure 11(a) form an envelope of data that are representative of the low energy environments responsible for surface charging while AE8, IGE 2006 and the "O'Brien 2007" aim at representing fluxes above a few hundreds of keV. In addition, the former are actual spectra while the latter are spectra constructed from different severe events. Guidelines such as *ECSS* [2008] and *NASA* [2011] are preferred to represent surface charging events. The ECSS and NASA guidelines define worst-case environments for surface charging in geosynchronous orbit. Designed for spacecraft engineering tools, these environments are provided in the form of Maxwellian distributions. Figure 12 presents the worst-case spectra taken from the design guidelines and the FE10k-15min worst-case spectrum, for (a) electrons and (b) protons. For immediate comparison of the LANL worst-case with guidelines, it also shows the ratio between the FE10k-15min worst-case and each of the guidelines worst-case spectra, for (c) electrons and (d) protons. The NASA worst-case, given by a single Maxwellian distribution approximation of the 90th percentile of GEO data, is referred as "NASA-HDBK-4002A" [*NASA*, 2011; *Purvis et al.*, 1984]. The NASA alternative worst-cases given by double Maxwellian distributions deduced from actual spectra, are referred as "Deutsch ATS-6", "Mullen 1" and "Mullen 2" [*Deutsch*, 1982; *NASA*, 2011; *Mullen et al. 1981a*, *Mullen et al. 1981b*]. The ECSS worst-case, given by a double Maxwellian distribution deduced from an actual spectrum, is referred as ECSS WC [*Gussenhoven and Mullen*, 1983; *ECSS*, 2008]. "ECSS WC", "Mullen 1" and "Mullen2" are double Maxwellian distribution fits of the same environment that was measured on SCATHA on April 24th, 1979 at 0650 UTC. The SCATHA potential reached -370 V when it was in sunlight, just before it reached -8 kV entering the Earth's shadow. Depending on the method used by the authors - either direct fitting of the curve or use of the distribution moments to compute the parameters [*Garrett and deForest*, 1979], it seems that different parameters have been extracted from this event. In this paper, we propose an additional triple Maxwellian distribution to fit this event based on the electron flux perpendicular to the magnetic field line presented in figure 6 of *Gussenhoven and Mullen* [1983]. It is referred as "3M Scatha 1979/4/24" in Figure 12. This figure also presents the electron spectral shape that produced negative charging on the Russian ELECTRO spacecraft. It is referred by "Novikov fourth group". *Novikov et al.* [*2006*] obtained four spectral shapes from soft environment not producing any surface charging (first group of spectra) to spectra with intensive high-energy component, for which the mean energy is more than 5 keV (fourth group of spectra), that resulted in charging not only in the Earth's shadow, but also on the sunlit arcs of the orbit.

Concerning the electron fluxes presented in Figure 12a and Figure 12c, the FE10k-15min worst case is close to the fourth group of spectra from *Novikov et al.* [2006], even though the comparison is only permitted up to 10 keV because the ELECTRO satellite was equipped with <10 keV particle detectors. There is less than a factor of 2 between them. The guidelines worst-case spectra significantly differ from the FE10k-15min environment. The

differential fluxes of the "ECSS WC","NASA-HDBK-4002A","Mullen 1","Mullen 2" and "Deutsch ATS 6" specifications cross the FE10k-15min spectra at two locations. The first and second crossing points are observed at low energy between 7 and 14 keV, and at high energy between 100 and 500 keV, respectively. From Figure 11a, the FE10k-15min differential flux decreases by 4 orders of magnitude between 100 and 500 keV. As a result, for the comparison between spectra, the most important part of the energy distribution is below 100 to 200 keV. The FE10k and the "Novikov 4th group" environments exceed the NASA and ECSS guidelines below 7-14 keV by a factor of 2 to 10. Between 14 keV and 100 keV, the FE10-15min worst case is lower than guidelines by a factor of 3 to 5 for the "NASA-HDBK-4002A" and "Deutsch ATS-6" spectra, and by a factor of up to 40 for the "ECSS WC", "Mullen 1" and "Mullen 2" spectra. Above 100 keV, the "ECSS WC", "Mullen 1" and "Mullen 2" spectra exceed the FE10k-15min spectrum by a factor of up to 150. Concerning the "ECSS WC" spectra, caution was advised by the original authors because the electron fit significantly exceeded the actual data above 20 keV [*Gussenhoven et al.* 1983]. This is clearly shown in Figure 13 that represents the original data, its double Maxwellian distribution fit given by *Gussenhoven et al.* [1983] and the "3M" fit. The "3M" fit better represents the ~10 keV and >20 keV electron fluxes than single or two-Maxwellian environments. This is why it is recommended to use tri-Maxwellian or kappa distributions. The "3M Scatha 1979/4/24" is also in better agreement with the LANL data. It exceeds the FE10k-15min worst-case by less than a factor of 4 between 3 and 100 keV, and by less than a factor of 25 above 100 keV. Finally, the FE10k energetic distribution tail, above 1 MeV is not reproduced by any Maxwellian distribution. This flux has, however, a limited impact on surface charging analysis since it is orders of magnitude lower than the flux around 200 keV.

From Figure 12b and Figure 12d, there is less dispersion in the proton fluxes given by the guidelines and by the FE10k-15min spectra. The main difference is observed above 100 keV with a maximum ratio of 40 at a maximum for the "ECSS WC", "Mullen 1" and "Mullen 2" spectra. On the other hand, the "Deutsch ATS-6" is up to 10 times smaller than other spectra between 10 and 100 keV.

Finally, the specifications above differ significantly from each other, which means that the complex 3D interactions of these electron and proton spectra with a spacecraft would result in very different charging levels depending on a) the geometry of the satellite and (b) the covering materials. In eclipse, the most important process is the electron emission under electron and proton impacts, both depending on the materials used and on the particle energy and incidence angle. In sunlight, it is also necessary to take into account the emission of electrons by photon impact associated with typical fluxes of 10^9-10^{10} $cm^{-2}s^{-1}sr^{-1}$. This is one order of magnitude larger than the integrated electron fluxes, even during the worst-case conditions. It should thus result in almost no charging while the spacecraft remains in sunlight. Photoelectrons are, however, emitted with energy lower than 10 eV typically, which makes them very sensitive to local barriers of potentials induced by differential charging. As a result, the location and resistivity of insulating surfaces is of prime importance for the assessment of absolute and differential charging in GEO. The response of a unique spacecraft must be assessed to the full set of environments to find the true worst-case. It is recommended that spacecraft designers should not rely upon some arbitrary criteria (such as highest current density) to justify a single environment. Detailed 3D simulations are required to estimate the ESD risks.

7. Conclusions

In this study we have analyzed 16 years of LANL data and contrasted them with POES data to determine a new set of severe GEO environments. We compared them with current guidelines for the assessment of worst-case surface charging. Our principal results are:

- Surface charging events are correlated with low energy electron fluxes between 10 and 50 keV. Significant and high ESD risk levels are reached when the electron flux between 10 and 50 keV exceed ~1×10^8 and ~2×10^8 $cm^{-2}s^{-1}sr^{-1}$, respectively.
- In sunlight, LANL spacecraft potential decreased down to -2 kV. In eclipse, high charging levels below -5 kV have been observed during tens of minutes. It is recommended to separate eclipse and non-eclipse charging data and to examine the most severe events for the two cases.
- A set of anomalies reported by *Choi et al.* [2011] is concomitant with events selected in this paper considering high fluxes of low energy electrons.
- A set of extreme LANL environments has been extracted to complete the list of available environments used by guidelines to assess worst-case satellite surface charging in GEO. These events are correlated to the declining phase of the solar cycle, to seasonal effects and to the geomagnetic activity. The FE10k worst-cases should promote large negative frame potential and possibly differential charging. LFHE and HFAE worst-cases aims at testing differential charging in reduced and enhanced radiation induced conductivity conditions, respectively.
- A triple Maxwellian distribution fit to the SCATHA event measured on April 24th, 1979 has been proposed to represent the data better than the current fits in the spacecraft charging guidelines.

It is important to stress that LANL spacecraft are spinning spacecraft, with a rotating period of 86 s. The proportion of surface area covered by high resistivity dielectrics (typically Kapton® or Teflon® thermal blanket outer layers, second surface mirrors and solar cell coverglasses) is higher on spinning spacecraft compared to 3-axis stabilized spacecraft designs in common use today. Indeed, recent spacecraft use large solar arrays with conductive graphite composite solar array substrates that are permanently shadowed and therefore actively collect large negative net charge from the environment. How the frame potential changes in response to the environment depends on the ratio between the shaded and sunlit exposed conductive surface area. As a result, the statistics on frame charging derived from the LANL data may underestimate the frequency or severity of frame charging that would be observed on 3-axis stabilized spacecraft.

For the future, we recommend assessing worst-case charging of 3-axis stabilized spacecraft using the LANL worst-cases presented in this paper, in complement to worst-case conditions from spacecraft design guidelines, both in sunlight, eclipse and eclipse exit. As it depends so much on its geometry and on its covering materials, the response of a unique spacecraft response must be assessed to the full set of environments to find the true worst-case for this unique spacecraft.

Acknowledgments

We thank David Rodgers, Keith Ryden, Henry Garrett and Richard Horne for their useful discussions. We also thank the reviewers for their helpful comments and suggestions. We acknowledge R. Friedel, G. Reeves, M. Thomsen and M. Henderson from the Los Alamos National Laboratory for the provision of the LANL data used in this study.

The LANL data up until 2007 are publicly available on demand from Mike Henderson. The POES data used in this study are available from: https://www.ngdc.noaa.gov/stp/satellite/poes/dataaccess.html. The Kp index is available from https://omniweb.gsfc.nasa.gov/html/ow_data.html. The solar wind and IMF parameters and the AE and Dst indices were obtained from the OMNIWeb service of the Space Physics Data Facility at the Goddard Space Flight Center (http://omniweb.gsfc.nasa.gov/).

This research has been funded by 2015-2017 CNES R&D program. Part of the research leading to these results has received funding from the European Union Seventh Framework Programme (FP7/2007-2013) under grant agreement 606716 (SPACESTORM) and the Natural Environment Research Council Highlight Topic grant NE/P10738X/1 (Rad-Sat).

References

Baker, D. N. (2000), The occurrence of operational anomalies in spacecraft and their relationship to space weather, IEEE Trans. on Plasma Science, 28, 2007–2016.

Bame, S. J., D. J. McComas, M. F. Thomsen, B. L. Barraclough, R. C. Elphic, J. P. Glore, J. T. Gosling, J. C. Chavez, E. P. Evans, and F. J. Wymer (1993), Magnetospheric plasma analyzer for spacecraft with constrained resources, Rev. Sci. Instr., 64, 1026.

Belian, R. D., G. R. Gisler, T. Cayton, and R. Christensen (1992), High-Z energetic particles at geosynchronous orbit during the great solar proton event series of October 1989, J. Geophys. Res., 97, 16,897.

Bortnik, J., R. M. Thorne, and N. P. Meredith (2007), Modeling the propagation characteristics of chorus using CRRES suprathermal electron fluxes, J. Geophys. Res., 112, A08204, doi:10.1029/2006JA012237.

Cho, M., and D. E. Hastings (1993), Computer particle simulation of high voltage solar array arcing onset, J. Spacecr. Rockets, vol. 30, no. 2, pp. 189–201

Cho, M., and Y. Nozaki (2005), Number of Arcs Estimated on Solar Array of a Geostationary Satellite, J. Spacecraft and Rockets, Vol. 42, No. 4.

Cho, M. (2005), Failure mechanisms and protection methods of spacecraft power systems, International Symposium on Electrical Insulating Materials, Kitakyushu, Japan, 2005. 10.1109/ISEIM.2005.193320

Choi, H.-S., J. Lee, K.-S. Cho, Y.-S. Kwak, I.-H. Cho, Y.-D. Park, Y.-H. Kim, D. N. Baker, G. D. Reeves, and D.-K. Lee, (2011), Analysis of GEO spacecraft anomalies: Space weather relationships, Space Weather, 9, S06001, doi:10.1029/2010SW000597.

Choi, H.-S., J. Lee, K.-S. Cho, Y.-S. Kwak, I.-H. Cho, Y.-D. Park, Y.-H. Kim, D. N. Baker, G. D. Reeves, and D.-K. Lee (2012), Reply to comment by Joseph E. Mazur and T. Paul O'Brien on "Analysis of GEO spacecraft anomalies: Space weather relationships", Space Weather, 10, S03004, doi:10.1029/2012SW000765.

Davis, V. A., Mandell, M. J., and Thomsen, M. (2008), Representation of the Measured Geosynchronous Plasma Environment in Spacecraft Charging Calculations," Journal of Geophysical Research, Vol. 113, No. A10, Paper A10204. doi:10.1029/2008JA013116.

DeForest, S. E. (1972), Spacecraft charging at synchronous orbit, J. Geophys. Res., 77(4), 651–659.

DeForest, S. E. (1973), Electrostatic potentials developed by ATS-5, in Photon and Particle Interactions with Surfaces in Space, edited by R. J. L. Grard, pp. 263–267, Springer, Netherlands.

Deutsch, M.-J. C. (1982), Worst Case Earth Charging Environment, J. Spacecraft, Vol. 19, No. 5, AIAA 82-4223.

ECSS (2008), ECSS-E-ST-10-04C, Space environment (http://ecss.nl/standard/ecss-e-st-10-04c-space-environment/)

Ferguson, D. C., and I. Katz (2014), The Worst-Case GEO Environment and the Frequency of Arcs in GEO, in Proceedings of Spacecraft Charging Technologies Conference, Pasadena, CA 2014. DOI: 10.1109/TPS.2015.2432718

Ferguson, D.C., R.V. Hilmer and V. A. Davis (2015), The best GEO daytime spacecraft charging index, Journal of Spacecraft and Rockets, Vol. 52, No. 2, pp. 526-543. https://doi.org/10.2514/1.A32959

Ferguson, D.C. (2016), Oops! We have a problem! Spacecraft charging related anomalies from DSCS-II to GPS, Dale C. Ferguson, 14th Spacecraft Charging Technology Conference, ESA/ESTEC, Noordwijk, NL, 04-08 April 2016 (http://old.esaconferencebureau.com/2016-events/14sctc/proceedings)

Garrett, H. B., and S. E. de Forest (1979), An analytical simulation of the geosynchronous plasma environment, Planet. Space Sci., Vol. 27, pp. 1101-1109.

Garrett, H. B. (1981), The charging of spacecraft surfaces, Rev. Geophys., 19(4), 577–616, doi:10.1029/RG019i004p00577.

Gussenhoven, M.S. and E. G. Mullen (1983), Geosynchronous environment for severe spacecraft charging, J. Spacecraft and Rockets 20, N°1, p. 26.

Iucci, N., et al. (2005), Space weather conditions and spacecraft anomalies in different orbits, Space Weather, 3, S01001, doi:10.1029/2003SW000056.

Koons, H. C., J. E. Mazur, R. S. Selesnick, J. B. Blake, J. F. Fennell, J. L. Roeder, and P. C. Anderson (2000), The impact of the space environment on space systems, in Proceedings of the 6th Spacecraft Charging Technology Conference, p. 7, Air Force Res. Lab., Hanscom AFB, Mass. (http://www.dtic.mil/docs/citations/ADA376872)

Lai, S. T., (2012), Fundamentals of spacecraft charging: spacecraft interactions with space plasmas, Princeton University Press, New Jersey.

Lazaro, D., and A. Sicard-Piet (2011), Détermination historique pire cas d'environnement, ONERA RF 1/18484 DESP.

Leach, R. D (1995). Failures and anomalies attributed to spacecraft charging, NASA, Tech. Rep. NASA-RP-1375.

Maejima, H., S. Kawakita, H. Kusuwake, M. Takahashi, T. Goka, T. Kurosaki, M. Nakamura, K. Toyoda, M. Cho (2004), Investigation of Power System Failure of a LEO Satellite Investigation of Power System Failure of a LEO Satellite, 2nd International Energy Conversion Engineering Conference, Providence, RI, AIAA 2004-5657 (https://doi.org/10.2514/6.2004-5657)

Mandell, M. J., V. A. Davis, D. L. Cooke, A. Wheelock, C. J Roth (2006), Nascap-2k Spacecraft Charging Code Overview, IEEE Trans. Plasma Sci., Vol. 34, No. 5.

Matéo-Vélez, J.-C., A. Sicard-Piet, D. Lazaro, V. Inguimbert, P. Sarrailh, S. Hess,V. Maget and D. Payan (2016a), Severe Geostationary Environments: Numerical Estimation of Spacecraft Surface Charging from Flight Data, Journal of Spacecraft and Rockets, Vol. 53, No. 2, pp. 304-316. doi: 10.2514/1.A33376

Matéo-Vélez, J.-C., N. Ganuschkina, N. Meredith, A. Sicard-Piet, V. Maget, D. Payan, I. Sillanpaa and S. Dubyagin (2016b), From GEO/LEO environment data to the numerical estimation of spacecraft surface charging at MEO, 14th Spacecraft Charging and Technology Conference, Noordwijk, NL. (http://old.esaconferencebureau.com/2016-events/14sctc/proceedings)

Mazur, J. E., and T. P. O'Brien (2012), Comment on "Analysis of GEO spacecraft anomalies: Space weather relationships" by Ho-Sung Choi et al.", Space Weather, 10, S03003, doi:10.1029/2011SW000738.

Meier, M., R. D. Belian, T. E. Cayton, R. A. Christensen, B. Garcia, K. M. Grace, J. C. Ingraham, J. G. Laros, and G. D. Reeves (1996),The energy spectrometer for particles (ESP): Instrument description and orbital performance, in Proceedings of the Taos Workshop on the Earth's Trapped Particle Environment, edited by G. D. Reeves, AIP Conf. Proc., 383, 203 - 210.

Meredith, N. P., R. B. Horne, R. M. Thorne, D. Summers, and R. R. Anderson (2004), Substorm dependence of plasmaspheric hiss, J. Geophys. Res., 109, A06209, 10.1029/2004JA010387.

Meredith N.P., R. B. Horne, J. D. Isles, J. C. Green (2016), Extreme Energetic Electron Fluxes in Low Earth Orbit: Analysis of POES E > 30, E > 100 and E > 300 keV Electrons, Space Weather, doi: 10.1002/2015SW001348

Minow, J. I., and L. N. Parker (2014), Spacecraft charging: anomaly and failure mechanisms, Spacecraft Anomalies and Failures Workshop, Chantilly, VA (https://ntrs.nasa.gov/archive/nasa/casi.ntrs.nasa.gov/20140012586.pdf)

Mizera, P.P. (1981), Charging Results from the Satellite Surface Potential Monitor, Journal of Spacecraft and Rockets, Vol. 18, No. 6, pp. 506-509. https://doi.org/10.2514/3.57848

Mullen, E.G., M. S. Gussenhoven, H. B. Garrett (1981a), A 'Worst Case' Spacecraft Charging Environment as Observed by SCATHA on 24 April 1979. AFGL-TR-81-0231.

Mullen, E.G., D.A. Hardy, H. B. Garrett and E. C. Whipple (1981b). P78-2 SCATHA Environmental Data Atlas, Spacecraft Charging Technology. 1980. NASA CP-2182/AFGL-TR-81-0270.

Mullen, E.G., M. S. Gussenhoven, D.A. Hardy (1986), SCATHA Survey of High-Level Spacecraft Charging in Sunlight, Journal of Geophysical Research, vol. 91, no. A2, 1474-1149.

Muranaka, T. , S. Hosoda, J. Kim, S. Hatta, K. Ikeda, T. Hamanaga, M. Cho, H. Usui, H. O. Ueda, K. Koga and T. Goka (2008), Development of multi-utility spacecraft charging tool (MUSCAT), IEEE Trans. Plasma Sci., Vol 36, N°5.

NASA (2011), NASA-HDBK-4002A, Mitigating In-Space Charging Effects—A Guideline.

Novikov, L. S. , V.N. Mileev, K.K. Krupnikov, A.A. Makletsov, B.V. Marjin, M.O. Rjazantseva, V.V. Sinolits and N.A. Vlasova (2008), Simultaneous investigation of magnetospheric plasma and spacecraft charging, Advances in Space Research 42, 1307–1312

O'Brien, T. P., J. F. Fennell, J. L. Roeder, and G. D. Reeves (2007), Extreme electron fluxes in the outer zone, Space Weather, 5, S01001, doi:10.1029/2006SW000240.

Oda, M., M. Nakamura and M. Cho (2016), Analysis of dense-electron-induced spacecraft charging in geosynchronous orbit, Proc. 14th Spacecraft Charging and Technology Conference, Noordwijk, NL. (http://old.esaconferencebureau.com/2016-events/14sctc/proceedings)

Payan, D., F. Séverin, J.-P. Catani, J.-F. Roussel, R. Reulet, and D. Sarrail (2001), Electrostatic discharges on solar arrays. Physical model of inverted potential gradient electrostatic discharge, Proc. 7th Spacecraft Charging Technology Conference, Noordwijk, The Netherlands. (http://adsabs.harvard.edu/full/2001ESASP.476..151P)

Purvis C. K. (1983), The role of potential barrier formation in spacecraft charging, NASA-TM-83500

Purvis C. K., H. B. Garrett, A. C. Whittlesey and N. J. Stevens (1984), Design Guidelines for Assessing and Controlling Spacecraft Charging Effects, NASA Technical Paper 2361.

Raeder, J., Y.L. Wang, T.J. Fuller-Rowell and H.J. Singer (2001), Global simulation of magnetospheric space weather effects of the Bastille day storm, Sol Phys, 204: 323. doi:10.1023/A:1014228230714

Rodgers, D., A. Hilgers, F. Cipriani, J.-C. Mateo-Velez, D. Payan, H. Wulf, C. Imhof, D. Pitchford and H. Zugaj (2016), Critical review of spacecraft charging standards, Proc. 14th Spacecraft Charging and Technology Conference, Noordwijk, NL. (http://old.esaconferencebureau.com/2016-events/14sctc/proceedings)

Roussel, J.-F. , G. Dufour, J.-C. Mateo-Velez, B. Thiébault, B. Andersson, D. Rodgers, A. Hilgers and D. Payan (2012), SPIS multi time scale and multi physics capabilities: development and application to GEO charging and flashover modelling, IEEE Trans. Plasma Sci., Vol 40, N°2

Russell, CT, and R. L. McPherron (1973), Semiannual variation of geomagnetic activity, Journal of Geophysical Research 78.1, 92-108.

Ryden, K. A. and A. D. P. Hands (2017), Modeling of Electric Fields Inside Spacecraft Dielectrics Using In-Orbit Charging Current Data, IEEE Trans. Plasma Science, 99, doi: 10.1109/TPS.2017.2665622

Sarno-Smith, L. K., B. A. Larsen, R. M. Skoug, M. W. Liemohn, A. Breneman, J. R. Wygant, and M. F. Thomsen (2016), Spacecraft surface charging within geosynchronous orbit observed by the Van Allen Probes, Space Weather, 14, 151–164, doi:10.1002/2015SW001345.

Sicard-Piet, A., S. Bourdarie, D. Boscher, H. W. Friedel, M. Thomsen, T. Goka, T. et al. (2008), A new international geostationary electron model: IGE-2006, from 1 keV to 5.2 MeV, Space Weather, 6, S07003. doi:10.1029/2007SW000368.

Thiebault, B., B. Jeanty-Ruard, P. Souquet, J. Forest, J.-C. Mateo Velez, P. Sarrailh, D. Rodgers, A. Hilgers, F. Cipriani, D. Payan and N. Balcon (2016), SPIS 5.1, an innovative approach for spacecraft plasma modelling, IEEE Transactions on Plasma Science, Vol 43, pp 2782-2788. doi: 10.1109.TPS.2015.2425300

Thomsen, M., E Noveroske, JE Borovsky, DJ McComas (1999), Calculation of Moments from Measurements by the Los Alamos Magnetosphere Plasma Analyzer, Los Alamos National Lab. Rept. LA-13566-MS, Los Alamos, NM, 1999.

Thomsen, M. F., M. G. Henderson, and V. K. Jordanova (2013), Statistical properties of the surface-charging environment at geosynchronous orbit, Space Weather, 11, 237–244, doi:10.1002/swe.20049.

Vette, J. I. (1991), The AE-8 trapped electron model environment, NASA-TM-107820.

Wilkinson, D. C., National Oceanic and Atmospheric Administration's spacecraft anomaly data base and examples of solar activity affecting spacecraft, Journal of Spacecraft and Rockets, v 31,160-165, 1994.

Wrenn, G. L. (1995), Conclusive evidence for internal dielectric charging anomalies on geosynchronous communications spacecraft, J. Spacecr. Rockets, 32, 514-520

Wrenn, G. L. , D. J. Rodgers, and K. A. Ryden (2002), A solar cycle of spacecraft anomalies due to internal charging," Ann. Geophys., vol. 20, no. 7, pp. 953–956.

Table 1 - List of the LANL satellites used in this study, together with the time periods covered by MPA, SOPA and ESP detectors

LANL SC	1989-046	1990-095	1991-080	1994-084	97A	02A
from	Sept 1989	Jan 1991	Dec 1991	Dec 1994	Jul 1997	Jan 2002
to	Apr 2001	Nov 2005	Nov 2004	Nov 2005	Nov 2005	Nov 2005

Table 2 – Characteristics of LANL top 100 events considering 15 minutes averaged environments for FE10k, HFAE and LFHE. PG5k fluxes are averages over the full duration of the event, *i.e.* when consecutive potentials are below -5 kV.

	8 keV differential flux	10-50 keV integral flux	Min, Max, Average potential
	$\times 10^3$ $cm^{-2}.s^{-1}.sr^{-1}.eV^{-1}$	$\times 10^8$ $cm^{-2}.s^{-1}.sr^{-1}$	V
FE10k (15 min)	4 to 20	1.2 to 2.0	-1900, -20, -600
HFAE (15 min)	2 to 19	0.2 to 1.4	-8600, -30, -800
LFHE (15 min)	6 to 27	0.5 to 1.6	-5800, -20, -500
PG5k	3 to 40	0.15 to 1.2	-8700, -5000, -6000

Table 3 – Concomitancy between anomalies reported in *Choi et al.* [2011] with LANL severe events. The group each anomaly is more likely to belong to is indicated in parenthesis: (1) internal charging caused by electrons of energy above 100's of keV (while at the same time not being able to rule out single event effects generated by solar ions above a few MeVs), (2) surface charging caused by electrons of energy below 10's of keV

List of anomalies from *Choi et al.* [2011]										Concomitant LANL events								
Number	Date			UT		LT		Kp	Satellite	Anomaly	LANL Satellite	Date			UT		LT	kp	Pot (V)	top 100
1	11	Jan	1997	11	15	05	21	6	Telstar 401	Electrostatic discharge; total loss (2)	LANL_1990_095	12	Jan	1997	8	16	5.9	4.7	-225	HFAE N°50
13	1	Sep	1998					5	Sirius 2	Loss of some solar cells (2)	LANL_1994_084	1	Sep	1998	16	58	23.8	4	-4700	LFHE N°2
22	30	Jul	1999					8	Anik E2	Temporary outage (1)	LANL_1994_084	30	Jul	1999	20	11	3.2	7.7	-900	FE10k N°64
24	12	Sep	1999					6	PAS-8	Temporary outage (1)	LANL_1994_084	12	Sep	1999	18	52	1.9	6	-850	LFHE N°4
35	23	Oct	2001					8	Echostar VI	Loss of two solar array strings (of a total of 112) announced (2)	LANL_LANL_97A	23	Oct	2001	00	18	5	5.3	-70	LFHE N°48
43	19	Sep	2003	12	56	07	00	7	Telstar 4	Shut down after a short circuit of its primary power bus, total loss (2)	LANL_1994_084	19	Sep	2003	18	43	4.5	4.7	-200	HFAE N°19
											LANL_1991_080	17	Sep	2003	10	21	23.4	6.3	-7200	PG5k N°3
											LANL_1994_084	22	Sep	2003	14	13	24	3.3	-8300	PG5k N°12
45	28	Oct	2003					5	Kodama (DRTS)	Temporary safe mode, triggered by increased noise received by Earth sensor. Recovered 7 Nov 2003 (1)	LANL_1994_084	29	Oct	2003	20	04	6	8.7	-950	FE10k N°5
55	17	Jan	2005	12	26	22	26	6	JCSat 1B	Thruster anomaly, temporary outage (1)	LANL_LANL_97A	18	Jan	2005	15	13	0.9	5.3	-2000	FE10k N°10
56	5	Apr	2005					7	Garuda 1	Almost complete loss of power, unknown reason (2)	LANL_1994_084	6	Apr	2005	11	31	0.4	2	-750	HFAE N°62
58	22	Jul	2005	06	32	16	32	5	JCSAT 1B	Loss of attitude (1)	LANL_LANL_02A	21	Jul	2005	0	15	5	5	-100	HFAE N°32
											LANL_1994_084	21	Jul	2005	9	27	22	2.3	-950	HFAE N°85
60	14	Sep	2005					7	Koreasat 2	90 min outage caused by attitude loss (1)	LANL_1994_084	15	Sep	2005	15	15	4.3	7	-950	FE10k N°6

Table 4 – Characteristics of the LANL worst-case environments

	SC	Date UTC	local time	Kp	8 keV diff. flux	10-50 keV integral flux	Potential
					$\times 10^3$ cm^{-2}.s^{-1}.sr^{-1}.eV^{-1}	$\times 10^8$ cm^{-2}.s^{-1}.sr^{-1}	V
FE10k-15min	LANL_1994_084	2004/4/5 19:21:19	0500	6.3	17	1.9	-670
FE10k-86sec	LANL_1994_084	2005/5/15 06:36:11	1930	8.3	35	3.2	-20
HFAE-15min	LANL_1994_084	2003/5/29 15:01:06	0045	7.7	6	1.1	-1500
HFAE-86sec	LANL_1994_084	2000/7/15 14:50:42	2130	8	10	2.0	-1600
LFHE-15min	LANL_1994_084	1997/9/3 20:19:06	0320	5	23	1.6	-500
LFHE-86sec	LANL_1989_046	1990/7/28 14:01:34	0245	6.7	19	2.1	-700
PG5k-46min	LANL_1991_080	1997/3/13 19:04:22	2330	2.3	9	0.2	-5500

Table 5 – Triple Maxwellian distribution parameters used to fit the LANL worst-cases environments and the SCATHA event measured on April 24th, 1979

	FE10k-15min	FE10k-86sec	HFAE-15min	HFAE-86sec	LFHE-15min	LFHE-86sec	PG5k	3M Scatha 1979/4/24
Electron								
density (cm-3)								
N1	0.5	1	0.05	0.1	0.25	0.7	0.4	0.2
N2	0.6	1.5	0.2	0.3	1	1	0.1	2
N3	0.2	0.25	0.25	0.4	0.05	0.001	0.004	0.01
temperature (keV)								
T1	1	0.5	0.5	1	0.5	1	5	0.1
T2	6	5	5	5	5	7	10	10
T3	15	15	20	20	10	20	30	50
Proton								
density (cm-3)								
N1	0.1	1.0	0.2	0.05	0.2	0.15	0.03	1
N2	1	2.0	0.35	0.4	1.1	1.5	0.5	1
N3	0.01	0.3	0.15	0.5	0.007	0.004	0.005	0.05
temperature (keV)								
T1	0.7	2	2	0.5	1	1	2	3
T2	15	20	15	5	15	15	12	20
T3	40	60	40	40	40	50	40	40

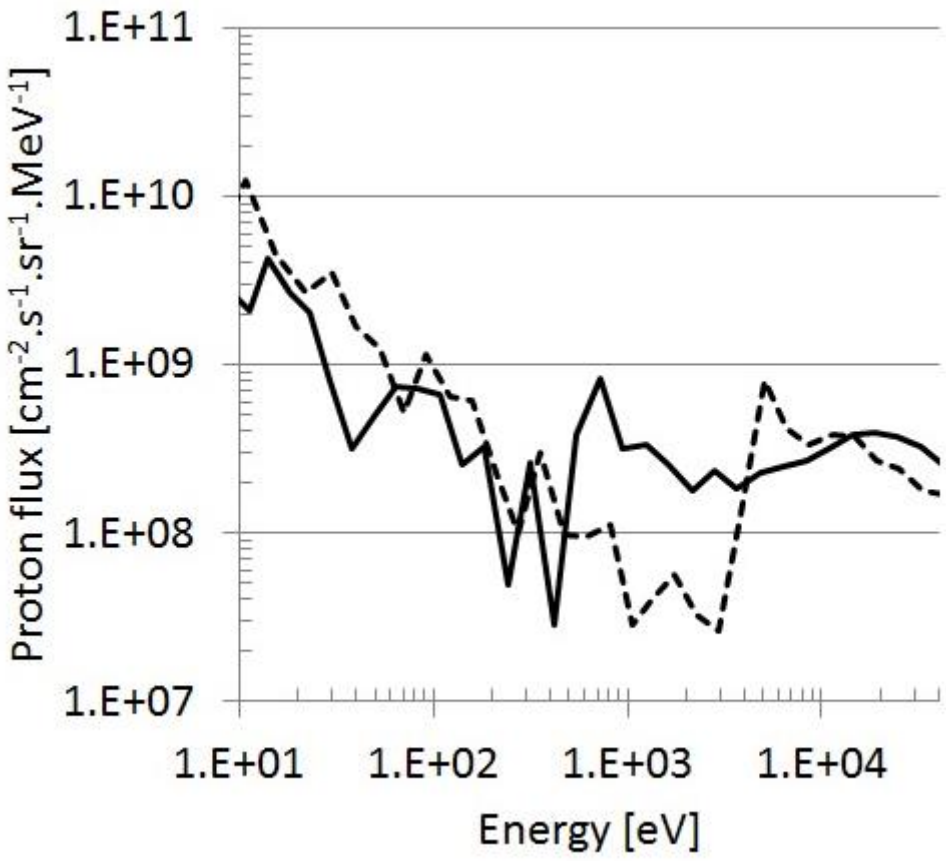

Figure 1 - Examples of proton differential fluxes measured on LANL satellites. The solid line was obtained on LANL_1994_084 on 2004/4/5 at 19:21:19' UTC. The dashed line was obtained on LANL_1991_080 1997/3/13 at 19:04:22 UTC

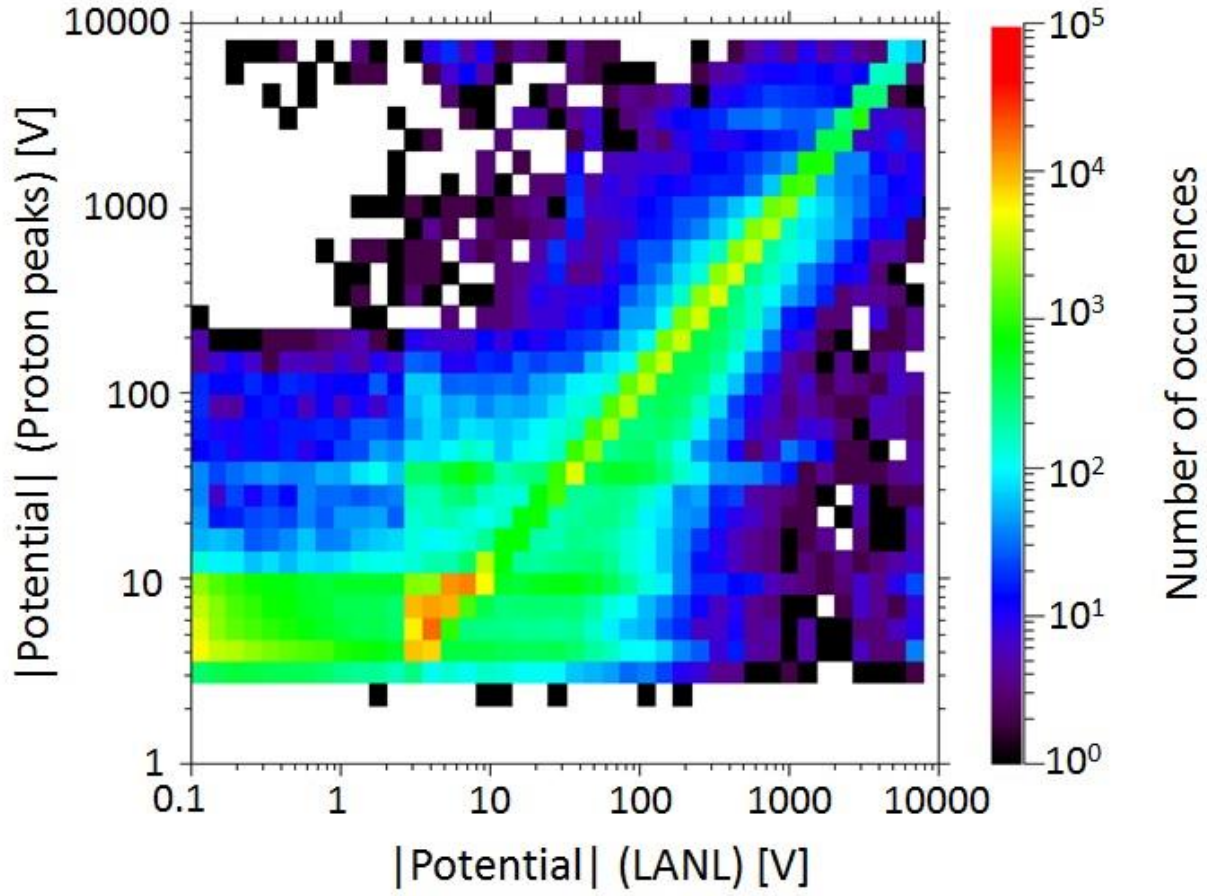

Figure 2 - Map of potentials given by the LANL routine and by the ion peak method over 16 years of LANL data. The color bar provides the number of occurrences of a given pair of potentials.

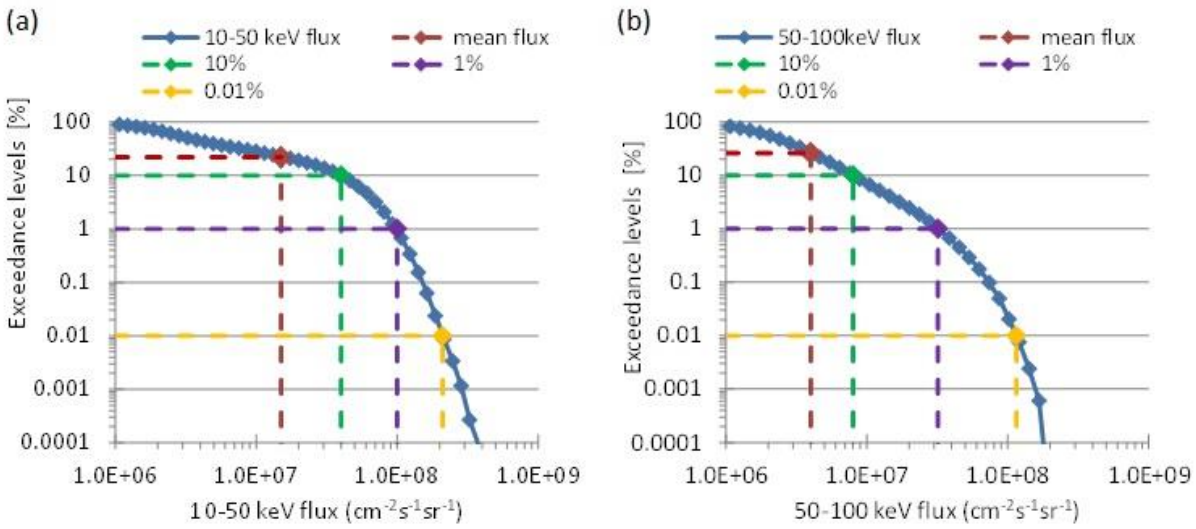

Figure 3 - Exceedance levels of electron fluxes between (a) 10 and 50 keV and (b) 50 and 100 keV. The mean flux and selected exceedance levels are highlighted by the colored lines

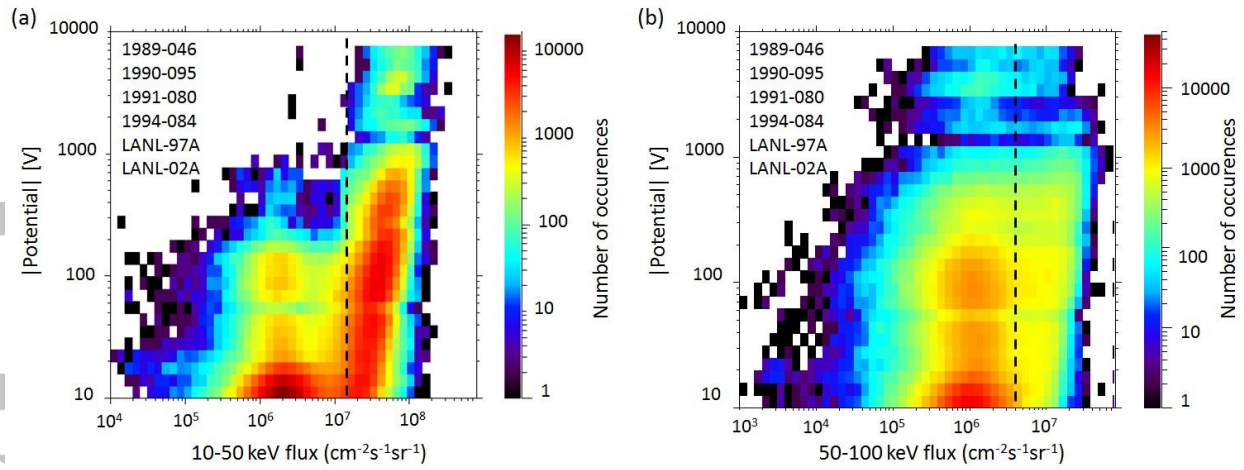

Figure 4 - Number of occurrences of pairs of a given negative potential and a given electron integral flux between (a) 10 and 50 keV and (b) 50 and 100 keV

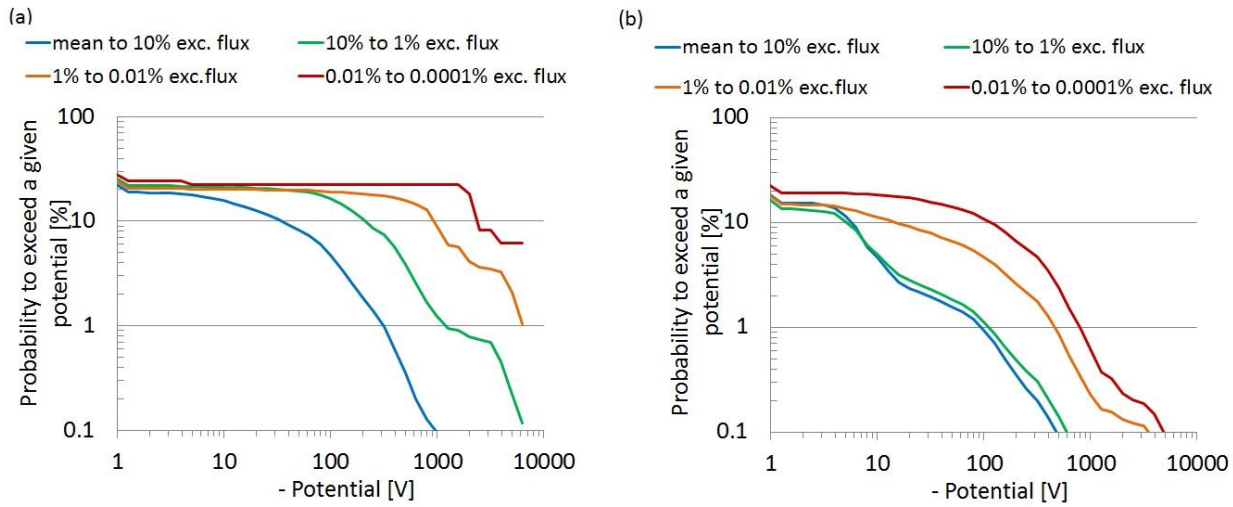

Figure 5 - Probability to reach a potential below a given potential for different ranges of integral fluxes between (a) 10 and 50 keV and (b) 50 and 100 keV

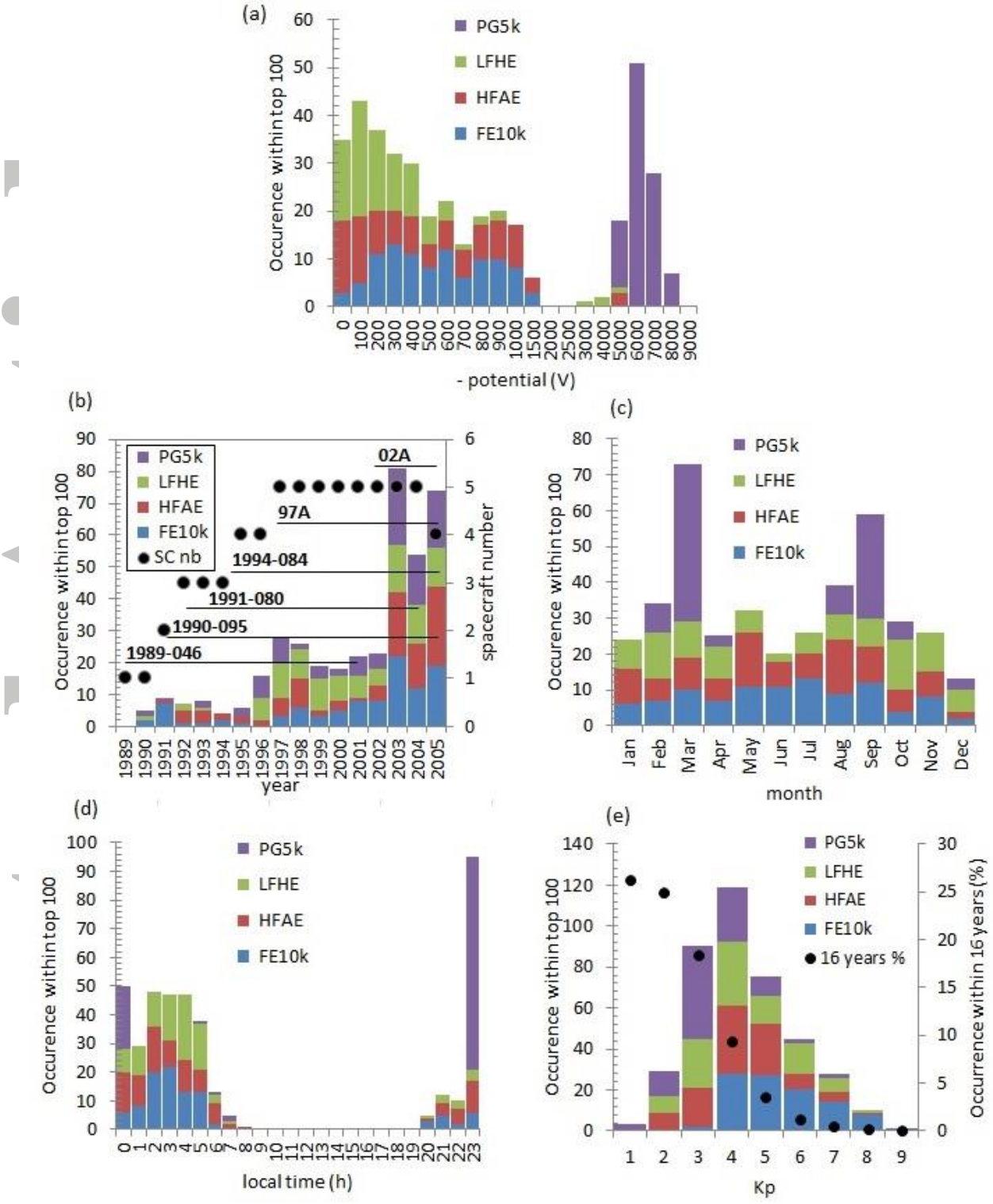

Figure 6 – Number of occurrences within the top 100 events, for each class of event (color-coded), as a function of (a) LANL spacecraft potential, (b) year, (c) month, (d) local time and (e) Kp index selected out of the 16 years of LANL data. The number of spacecraft hosting LANL sensors and their lifetime are also presented in (b). The relative occurrence frequency of the Kp index is also plotted in (e).

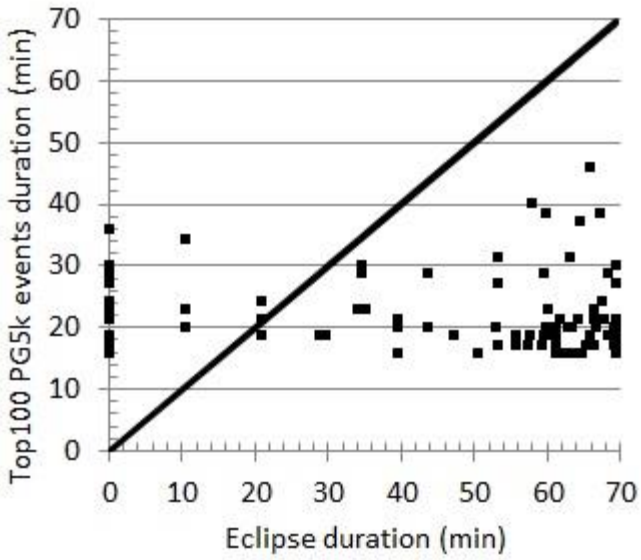

Figure 7 – Duration of PG5k top 100 events as a function of eclipse duration the same day

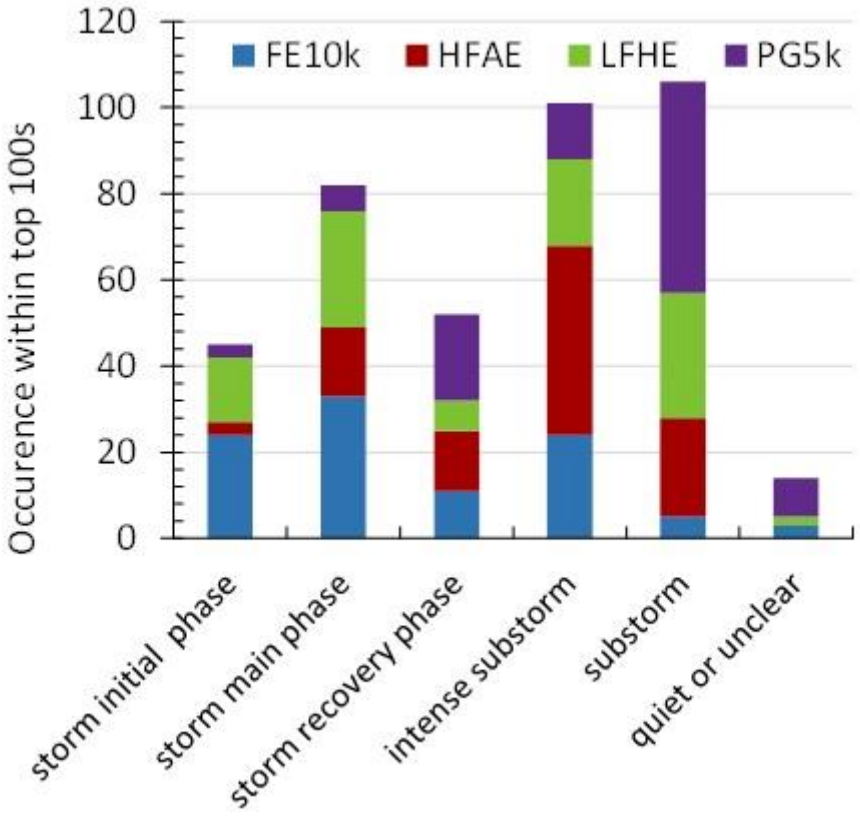

Figure 8 – Number of occurrences of storms and isolated substorms during the 400 selected LANL events

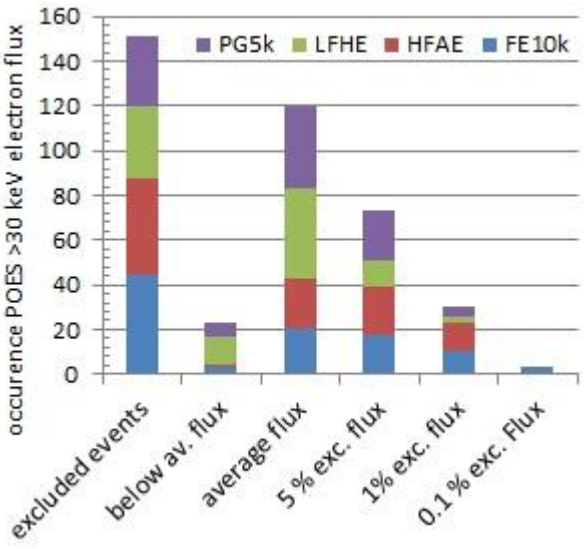

Figure 9 - Number of occurrences of NOAA/POES fluxes at LEO and at L*= ~6 during the FE10k, HFAE, LFHE and PG5k top 100 events

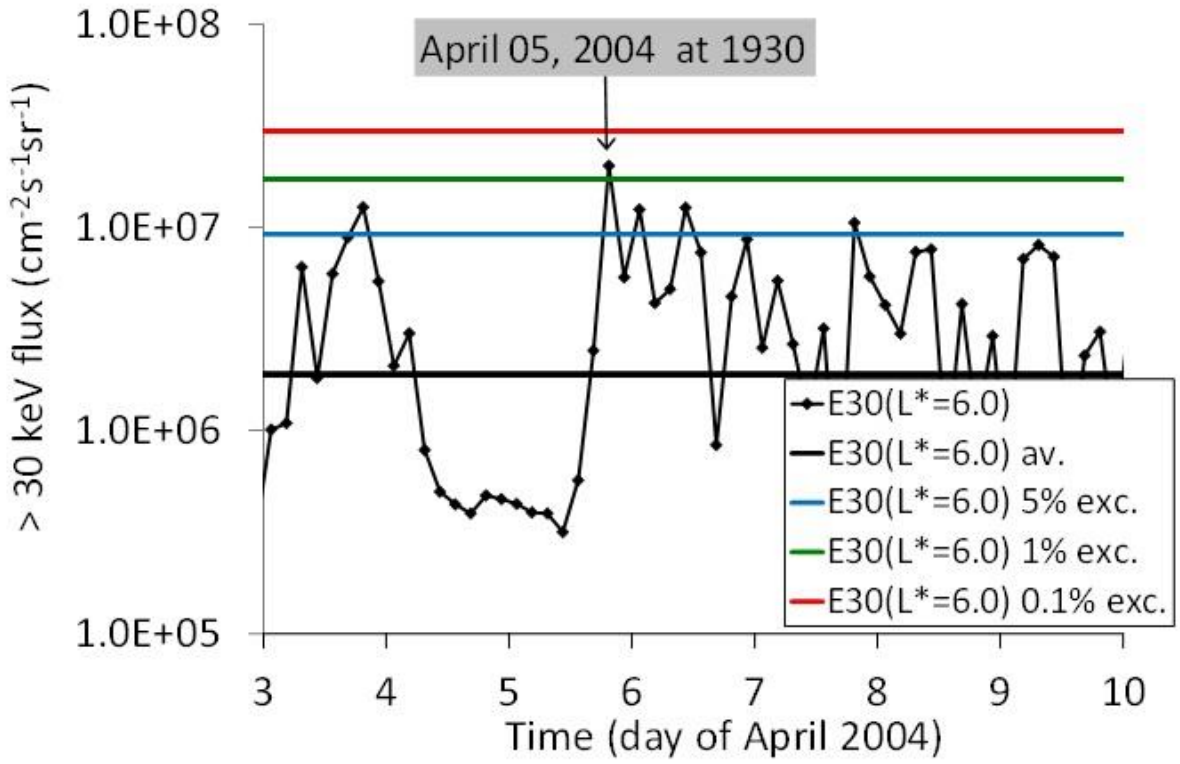

Figure 10 - Time evolution of the electron flux above 30 keV measured by NOAA/POES during the FE10k worst-case

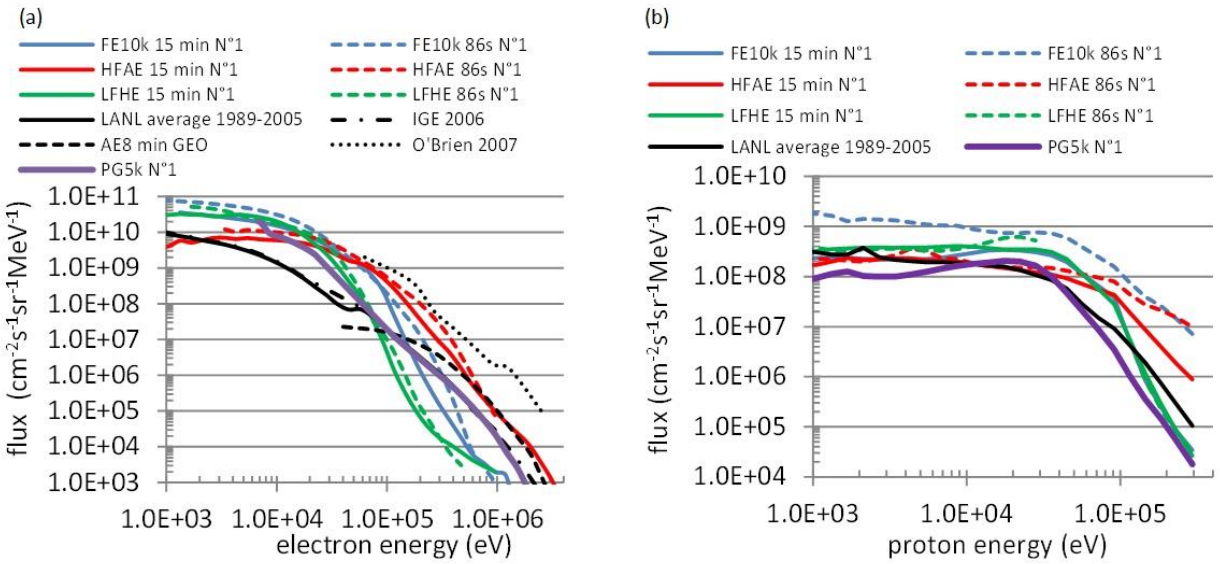

Figure 11 - (a) Electron and (b) proton differential fluxes during the worst case FE10k, HFAE, LFHE and PG5k events, compared to the average LANL flux, to the AE8 and IGE 2006 specifications and to the worst 1 hour interval reconstructed spectrum from *O'Brien et al.* [2007] concerning graph (a).

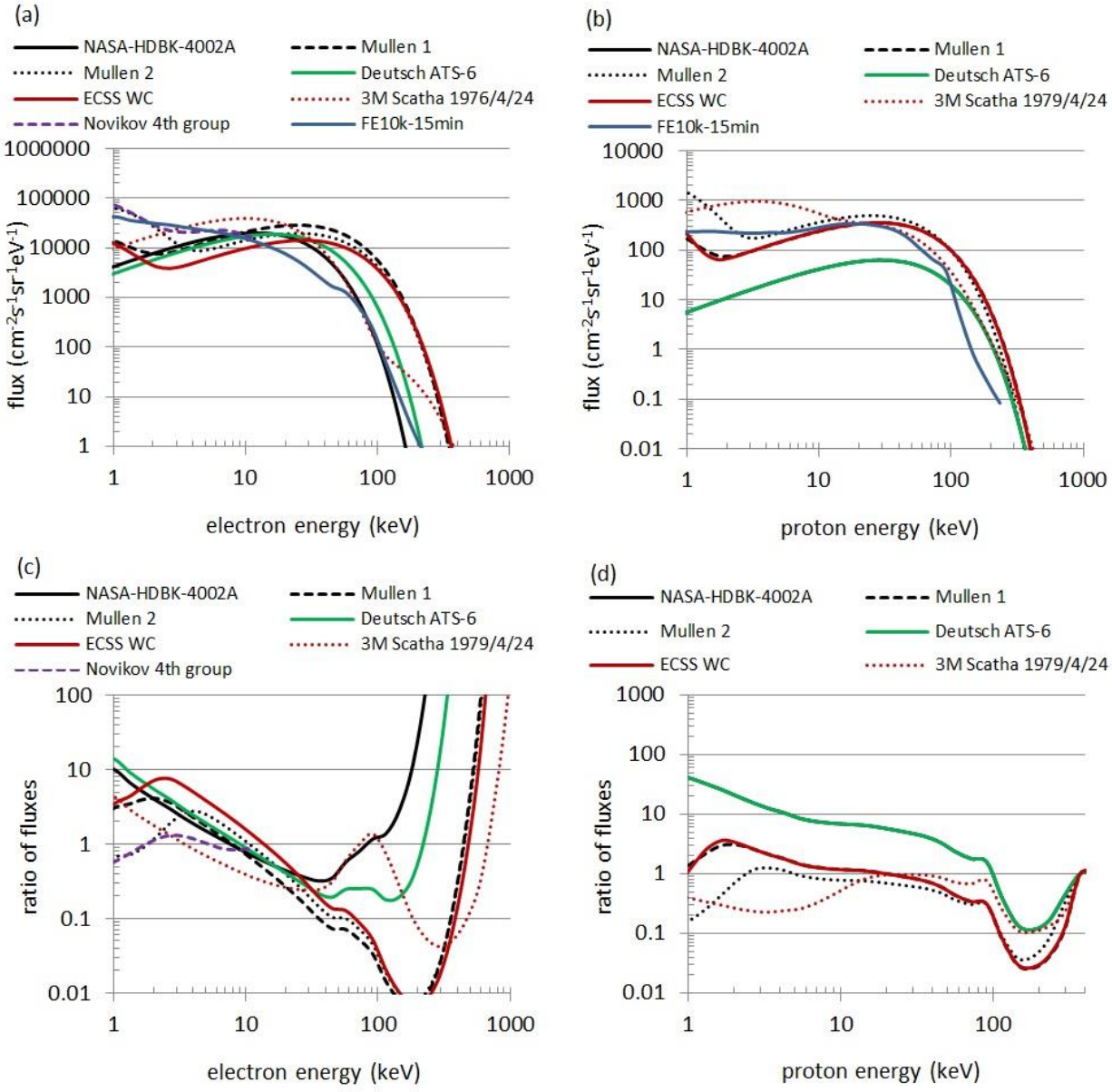

Figure 12 – Worst-case spectra from the literature and the FE10k-15min worst-case, for (a) electrons and (b) protons. Ratio of the FE10k over each of the guidelines worst-case, for (c) electrons and (d) protons.

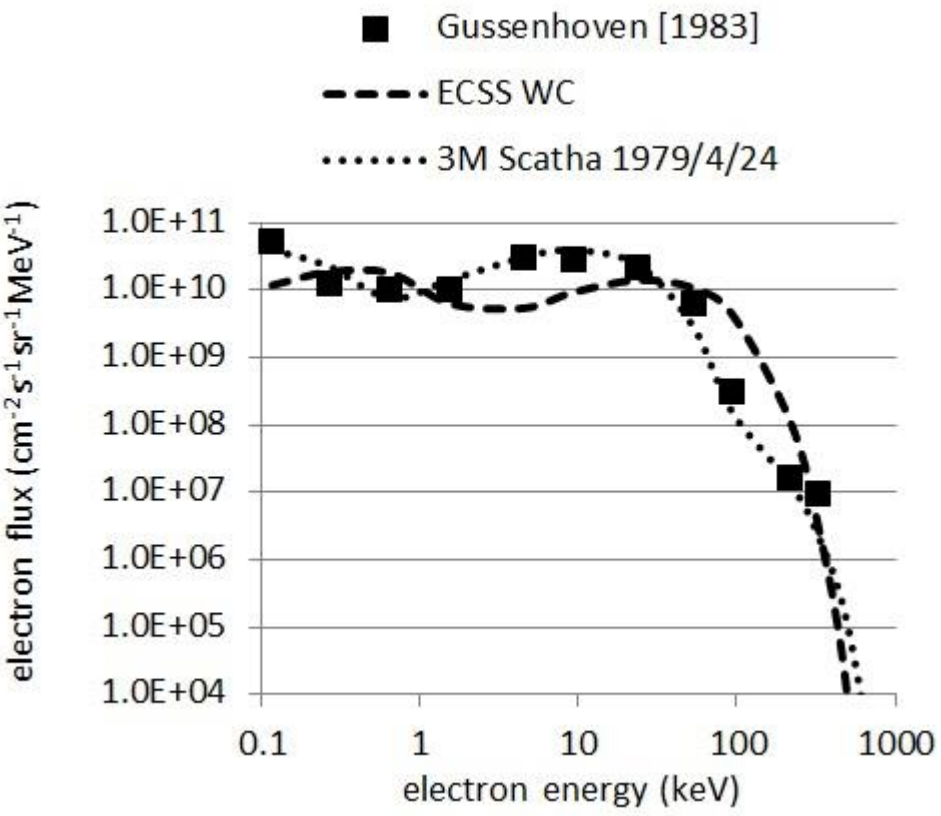

Figure 13 – Triple Maxwellian fit of the electron flux during the Scatha 1979/4/24 event compared to data extracted from the original paper by *Gussenhoven and Mullen* [1983] and to the ECSS worst-case environment